Materials & Design 252 (2025) 113824

Contents lists available at ScienceDirect

Materials & Design

journal homepage: www.elsevier.com/locate/matdes

In-situ alloying of nonequiatomic TiNbMoTaW refractory bio-high entropy alloy via laser powder bed fusion: Achieving suppressed microsegregation and texture formation☆

Yong Seong Kim [a], Ozkan Gokcekaya [a,b,*], Kazuhisa Sato [c], Ryosuke Ozasa [a,b], Aira Matsugaki [a,b], Takayoshi Nakano [a,b,*]

[a] Division of Materials and Manufacturing Science, Graduate School of Engineering, Osaka University, 2-1, Yamadaoka, Suita, Osaka 565-0871, Japan
[b] Anisotropic Design and Additive Manufacturing Research Center, Osaka University, 2-1, Yamadaoka, Suita, Osaka 565-0871, Japan
[c] Research Center for Ultra-High Voltage Electron Microscopy, Osaka University, 7-1, Mihogaoka, Ibaraki, Osaka 567-0047, Japan

ARTICLE INFO

Keywords:
High entropy alloys
Additive manufacturing
In-situ alloying
Crystallographic texture
Segregation

ABSTRACT

High-entropy alloys (HEAs) have attracted considerable attention owing to their excellent properties. However, the severe segregation of the constituent elements remains a common challenge in refractory HEAs. Recently, an approach to suppress segregation was proposed using laser powder bed fusion (LPBF) owing to the ultra-high cooling rates during solidification. Despite the advantages of LPBF, the persistent microsegregation between the dendritic and interdendritic regions of refractory HEAs and costly gas atomization process hinder the further development. To address these challenges, a novel nonequiatomic TiNbMoTaW refractory HEA was designed to minimize the difference between the liquidus and solidus temperatures to prevent segregation and phase separation for a better biological performance. In-situ alloying was implemented instead of costly and time-consuming gas atomization process. The segregation of constituent elements was suppressed by remelting, resulted in epitaxial growth and development of crystallographic texture, consequently reducing residual stress. The mechanical properties were improved due to the increase of solid solution strengthening and densification. It showed superior mechanical strength and equivalent biocompatibility compared to conventional biomaterials, indicating its superiority as a biomaterial. This study represents the first successful control of crystallographic texture through in-situ alloying of BioHEAs for next-generation biomaterials.

1. Introduction

High-entropy alloys (HEAs) represent a novel class of materials that deviate from traditional alloy concepts due to their composition of multiple principal elements [1,2], offering significant design flexibility [3–5]. As a result, HEAs are gaining attention as promising candidates for next-generation materials, particularly those that incorporate refractory elements. These HEAs are not only being explored for their high-temperature applications but are also emerging as potential biomaterials due to their non-toxic nature [6–8]. Specifically, HEAs containing refractory elements are distinguished by their exceptional strength [9–11], corrosion [12,13] and wear resistance [14,15], and biocompatibility [16,17], which are comparable to conventional biomaterials.

Most HEAs, such as arc-melted HEAs, are manufactured by casting. However, this approach has limitations, including phase separation by constituent element segregation [18,19] and the formation of intermetallic compounds [20–23]. These issues arise because of the relatively slow cooling rate inherent in casting processes (2×10^3 Ks^{-1}), compounded by the multicomponent nature of HEAs. Consequently, subsequent procedures such as heat treatment are required to establish and ensure the homogeneity of the constituent elements after the casting process.

Recently, research has been focused on producing HEAs using laser powder bed fusion (LPBF) as a promising additive manufacturing process to produce near-net-shaped components and modify the

☆ This article is part of a special issue entitled: 'Additive Manufacturing' published in Materials & Design.

* Corresponding authors at: Division of Materials and Manufacturing Science, Graduate School of Engineering, Osaka University, 2-1, Yamadaoka, Suita, Osaka 565-0871, Japan.
E-mail addresses: ozkan@mat.eng.osaka-u.ac.jp (O. Gokcekaya), nakano@mat.eng.osaka-u.ac.jp (T. Nakano).

https://doi.org/10.1016/j.matdes.2025.113824
Received 29 October 2024; Received in revised form 12 February 2025; Accepted 8 March 2025
Available online 9 March 2025

microstructure [24–26]. LPBF allows ultra-high cooling (10^5–10^7 Ks^{-1}), which can provide suppression of segregation of constituent elements [27–30]. Notably, this process streamlines production, eliminating the necessity for subsequent procedures, such as heat treatment for homogenization and machining, which can be challenging for HEAs, especially those containing refractory elements. While LPBF offers these advantages, challenges such as powder cost, oxidation during processing, and process optimization for defect-free refractory HEA fabrication must be addressed. Nevertheless, LPBF's capabilities make it a leading choice for advancing the development and application of challenging HEAs.

However, despite the advantages offered by LPBF, specific challenges still need to be resolved. The first challenge involves the persistence of microsegregation between the dendritic and interdendritic regions of constituent elements [31–34]. Despite the high cooling rate associated with LPBF, phase separation remains challenging [29]. Segregation of constituent elements inhibits solid solution strengthening, which is the primary strengthening mechanism of HEA [28]. Additionally, the segregation of constituent elements creates a potential difference on the surface, causing a decrease in corrosion resistance [35–37] and chemical inhomogeneity on the HEA surface preventing texture development and resulting in differences in cell adhesion [29]. Therefore, in order to reach the potential and demonstrate the unique properties of HEA, it is essential to suppress the segregation of constituent elements. In response to this challenge, we focus on the advantages of nonequiatomic HEAs in terms of design flexibility. The strategic approach of nonequiatomic HEAs has demonstrated the potential to enhance the inherent characteristics of equiatomic HEAs while affording greater latitude in design considerations [38–42]. Consequently, we have designed novel HEAs with exceptional attributes. A total of 29,790 composition combinations were calculated based on the melting points of the constituent elements. Among these, $Ti_1(NbMoTa)_2W_{0.5}$, simultaneously facilitated the formation of a single solid solution while effectively suppressing the segregation of the constituent elements [9].

The second challenge is the use of a pre-alloyed powder in the LPBF process. LPBF typically utilizes a pre-alloyed powder produced through gas atomization. However, this practice is associated with increased time, cost, and constraints on the versatility of alloy designs [43–45]. Furthermore, powder generated through gas atomization has been reported to induce elemental segregation [46–48], rendering it difficult for alloys based on refractory elements with high melting points. Segregation at the powder makes it difficult to achieve homogeneous element distribution in the as-built sample. Therefore, this study adopted an innovative approach to in-situ alloying that involves real-time alloying during the LPBF process. This method was used to overcome the limitations posed by the pre-alloy powders. The concept of in-situ alloying eliminates the necessity of preparing pre-alloyed powders instead utilizes using mixed powders. However, recent investigations in literature regarding in-situ alloying of HEAs have predominantly focused on blending a single type of powder with a pre-alloyed powder [43–45,49,50]. There is a need for research concerning in-situ alloyed HEA fabrication by LPBF employing a mixture of individual element powders. Additionally, the dissimilarity in melting points between elements poses a challenge for achieving uniform mixing [49,51–54]. However, recent studies have generally overlooked the melting point differences between constituent elements and have not applied specific strategies to suppress the segregation of these elements [55,56].

Morevoer, crystallographic texture control is a compelling characteristic of LPBF. Variations in LPBF process parameters produce the interplay of heat flow direction, thermal gradient (G), and solidification rate (R), inducing diverse grain morphologies and epitaxial growth, transitioning from equiaxed to columnar microstructures [57,58]. Crystallographic textures profoundly influence material properties, enhancing strength and ductility [59], Young's modulus [60,61], and corrosion resistance [62]. However, in the case of HEA, essential epitaxial growth for crystallographic texture control is impeded by constituent elements' segregation and phase separation [29]. Hence, the imperative lies in effectively mitigating constituent element segregation to govern crystallographic texture. Notably, to the best of our knowledge, crystallographic texture control has yet to be achieved in in-situ alloyed bio-high entropy alloy (BioHEA) utilizing mixed powders.

This study is the one of few reports challenging to fabricate refractory-based HEA fabricated by LPBF with in-situ alloy application of five elemental feedstock powders to achieve a single solid solution BioHEA. The innovative idea of this study is to overcome the segregation issue of in-situ alloying by alloy design and LPBF process parameter control. The novel non-equiatomic HEA alloy design strategy was focused on a minimized liquid-to-solid transformation temperature (ΔT) to suppress segregation with the contribution of the ultra-fast cooling rate nature of the LPBF process, thus, presenting this alloy as a good candidate to challenge the limitations of in-situ alloying in order to replace the traditional, expensive gas atomization process. Therefore, we fundamentally focused on alloy design to suppress segregation of constituent elements and designed a single solid solution BioHEA, that minimized the difference between the liquidus and solidus temperature. In addition, in-situ alloying using mixed powder was applied to take advantage of LPBF, which has an ultra-high cooling rate, while eliminating the disadvantages of high-cost pre-alloyed powder. Additionally, this study discusses crystallographic texture control, which is essential for the fabrication of low Young's modulus anisotropic materials to mimic Young's modulus of natural bone. We elucidated the underlying mechanism of texture formation based on the scan strategy and process parameters. This study represents a pioneering endeavor for crafting an in-situ alloyed BioHEA by LPBF featuring texture development.

2. Experimental procedures

2.1. Properties of elemental powders and mixing procedure

Ti powder (OSAKA Titanium Technologies, Japan), Nb powder (TANIOBIS GmbH, Germany), Mo powder (Avimetal AM, China), Ta powder (H. C. Starck, Germany), and W powder (Toshiba Materials, Japan) with purities higher than 99.5 % were used. The particle size distribution of each powder was measured using a Mastersizer 3000E (Malvern Panalytical, UK). D50 value of Ti, Nb, Mo, Ta, and W powders were 35 μm, 36 μm, 41 μm, 24 μm, and 8 μm, respectively. The five feedstock elemental powders were mixed using a rocking mixer (RM-10; Aichi, Japan) for 12 h to achieve homogeneity and its homogeneity was validated by compositional mapping analysis. The flowability of the mixed powder, shown in Fig. 1, was measured using a revolutionary powder analyzer (Mercury Scientific, USA).

The primary objective of designing this alloy was to effectively suppress the segregation of the constituent elements [9]. The

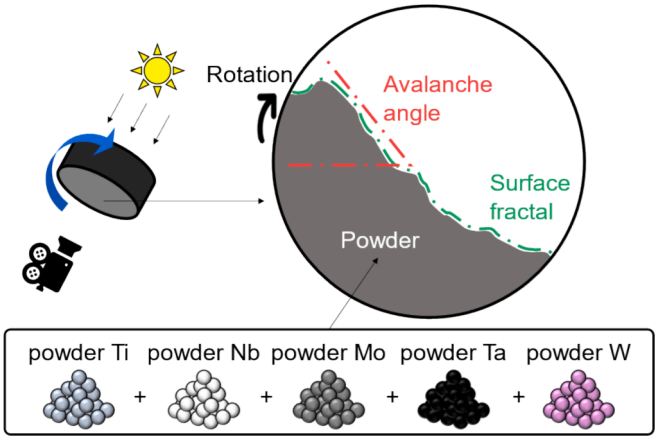

Fig. 1. Schematic representation of test for powder flowability.

composition was selected following this strategy: (1) To facilitate solid solution formation and mitigate segregation, the most critical parameters, atomic radius difference and mixing entropy [63,64], were first considered (indicated as S1 and S2 in Supp. Fig. S1). Consequently, Ti, Nb, Mo, Ta, and W were chosen as the constituent elements with similar atomic radius (Supp. Table S1) and pair entropy (Supp. Table S2). Additionally, each element does not exhibit cytotoxicity and is therefore widely used as a component of biomaterials [65–67]. (2) To ensure uniform melting during the in-situ alloying process, careful attention was given to minimizing the melting point difference. The specific composition of $Ti_X(NbMoTa)_YW_Z$ was calculated based on its melting point. The atomic radius and melting points used in these calculations are listed in Supp. Table S1. Among these compositions considering the difference between the solidus and liquidus temperature (ΔT, indicated as S3 in Supp. Fig. S1), $Ti_1(NbMoTa)_2W_{0.5}$, characterized by a small ΔT (22 °C), was selected. A small ΔT value represents an abbreviated solidification period, leading to the suppression of constituent element segregation during solidification [68]. The result of thermodynamic parameters and equilibrium phase diagram, Scheil–Gulliver solidification for $Ti_1(NbMoTa)_2W_{0.5}$ are shown in Supp. Table S3 and Supp. Fig. S2, respectively. Previously reported TiNbTaZrMo BioHEA showed a large ΔT of approximately 492 °C, and phase separation was observed due to segregation of constituent elements [18]. However $Ti_1(NbMoTa)_2W_{0.5}$ in this study showed a noticeably reduced ΔT compared to TiNbTaZrMo (Fig. S1 (a,e)), and as a result, segregation of constituent elements in $Ti_1(NbMoTa)_2W_{0.5}$ was suppressed in Scheil non-equilibrium simulations (Fig. S2 (b,c,d and f,g,h).

2.2. LPBF fabrication

In-situ alloyed Ti-Nb-Mo-Ta-W HEA samples with dimensions of 5 mm (depth) × 5 mm (length) × 5 mm (height) were manufactured using an LPBF machine (EOS M290, EOS, Germany). A single XY-scan strategy is used to rotate the scanning direction by 90° between the successive layers (Fig. 2 (a)). In a double XY-scan, each layer is remelted twice using the same process parameters and scan strategy, implementing the second scan to the already solidified layer, as shown in Fig. 2 (b). To reach a sufficient density of LPBF-process samples, various scan speeds and laser power were tried for fabrication. The optimized and comparative process parameters were determined as the conclusion of this excessive process parameter optimization. Some of these experimental studies were summarized in supplementary (Fig. S3-S5). From the established process window, scanning speeds of (v) 400 and 1000 mm/s were applied to each single and double XY-scan, denoted as S400, S1000, D400, and D1000. Under all conditions, the same laser power (P) of 240 W, hatch space (d) of 0.08 mm, and layer thickness (t) of 0.02 mm were applied. The volumetric laser energy density (VED) of the fabrication conditions is defined by Eq. (1).

$$VED = \frac{P}{vtd}[\mathrm{J/mm^3}] \tag{1}$$

The VED calculated using Eq. (1) was 375 J/mm^3 for the S400 and D400 samples and 150 J/mm^3 for the S1000 and D1000 samples. After each fabrication, powders were remixed for 12 h and same specimens were fabricated several times to ensure reproducibility. Additionally, we sieved the powder prior to remixing to prevent powder quality degradation due to process byproducts such as spatters.

2.3. Microstructure characterization

The relative densities ($relativedensity\% = 100\% - crackdensity\%$) [69] of the as-built samples obtained through in-situ alloying with LPBF were assessed using an optical microscope (OM; BX-60, Olympus, Tokyo, Japan) in the y-z plane. The relative density of each sample was measured using ImageJ software (version 1.53 k) and reported as an average of seven measurements. The phases of each powder and in-situ alloyed sample were investigated using X-ray diffraction (XRD; r X' pert PRO, Philips, Netherlands) with Cu Kα radiation. The microstructures and crystallographic textures were analyzed using a field-emission scanning electron microscope (FE-SEM; JIB-4610F, JEOL, Japan) equipped with an energy-dispersive X-ray spectrometer (EDS; X-MaxN, Oxford Instruments, UK) and electron backscatter diffraction system (EBSD; NordlysMax^3, Oxford Instruments, UK). Scanning transmission electron microscopy (STEM, JEM ARM200F, JEOL, Japan) was used to characterize elemental segregation at the nanoscale. Nano-hardness was measured using a nanoindentation tester (ENT-1100, Elionix Corp., Japan) with a test load of 15 mN (P_{max}) at a successive loading rate of 1 mN/s and held at P_{max} for 100 s. To evaluate the mechanical properties, a compression test (n = 3) was conducted on rectangular test samples measuring 2 mm × 2 mm × 5 mm using an Instron-type testing machine

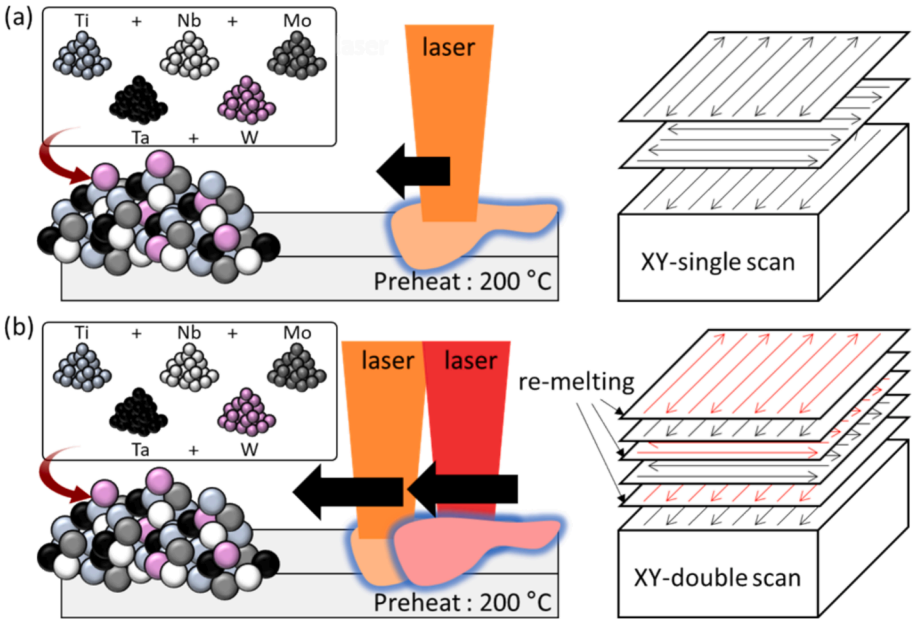

Fig. 2. Schematic representation of (a) single XY-scan and (b) double XY-scan.

(AG-X, Shimadzu, Japan) at a nominal strain rate of 1.67×10^{-4} s^{-1}. During the compression test, Young's modulus was measured by a non-contact extensometer (TRViewX, Shimadzu, Japan).

2.4. Biocompatibility

The biocompatibility assessment focused on cell adhesion, which was driven by molecular interactions between cells and the alloy surface. Square specimens with dimensions of 5 mm × 5 mm × 1 mm (n = 5) were prepared, and their surfaces were mirror polished. For comparison, commercially pure Ti (CP-Ti) and 316 L-type stainless steel (SUS316L) of the same size were prepared. Primary osteoblasts were extracted from the calvariae of neonatal mice using a sequential collagenase/trypsin digestion method. The isolated cells were diluted to a concentration of 10,000 cells/cm^2 and seeded onto the substrates. After 24 h of incubation in a humidified 5 % CO_2 atmosphere, the cells were fixed with methanol and stained with a 5 % aqueous Giemsa solution (FUJIFILM Wako Chemicals). The adhesion of osteoblasts to each substrate was examined under an optical microscope (BX60, Olympus). To visualize the cytoskeletal organization on the fabricated specimens, cells were fixed with 4 % paraformaldehyde, rinsed with phosphate-buffered saline containing Triton X-100, and incubated in normal goat serum to block non-specific antibody binding. The cells were then treated with anti-vinculin primary antibodies (Sigma), followed by incubation with secondary antibodies (Alexa Fluor 594 goat anti mouse IgG and Alexa Fluor 488 phalloidin, Thermo Fisher Scientific), and Hoechst 33,342 nuclear stain (Nacalai Tesque, Kyoto, Japan). ProLong Diamond reagent (Thermo Fisher Scientific) was used for mounting, and the cells were imaged using fluorescence microscopy (BZ-X710, Keyence). Quantitative results are expressed as mean ± standard deviation. Statistical significance was assessed using a two-tailed unpaired *t*-test by Tukey's post-hoc test, with a p-value < 0.05 considered statistically significant.

3. Results and discussion

Fig. 3 (a–e) show the particle shape and size distribution results for the Ti, Nb, Mo, Ta, and W powders, whereas Fig. 3 (f) shows the overall particle size distribution The particle size distribution of the W powder, of particular interest, was deliberately chosen to be small, considering its higher melting point compared with other elements. The selection of mixed-size powders ensures a uniform distribution by increasing the powder bed packing density with small W powder taking the space in between large powders and enhancing laser absorption efficiency, leading to more uniform melting [70–73]. And the effectiveness of the mixing process was validated using EDS (Fig. 3 g1–g6). The fluidity of the mixed powder was evaluated and compared with that of commercial Ti-6Al-4V spherical powders, which exhibited acceptable flowability (Table 1) considering the random shape of Ta powders. Besides, this process allows mixing different size of powders to homogenize the distribution of the mix while not causing any damage to the powders. Moreover, rocking mixer has advantages over ball milling and gas atomization processes considering the equipment, operational cost, and

Table 1
Characterization of mixed powder for in-situ alloying and Ti-6Al-4V commercial powder in terms of flowability.

	Avalanche Angle [°]	Rest angle [°]	Surface fractal
$Ti_1(NbMoTa)_2W_{0.5}$ mixed powder	48.4	35.4	1.85
Ti-6Al-4V commercial powder	39.2	30.7	1.73

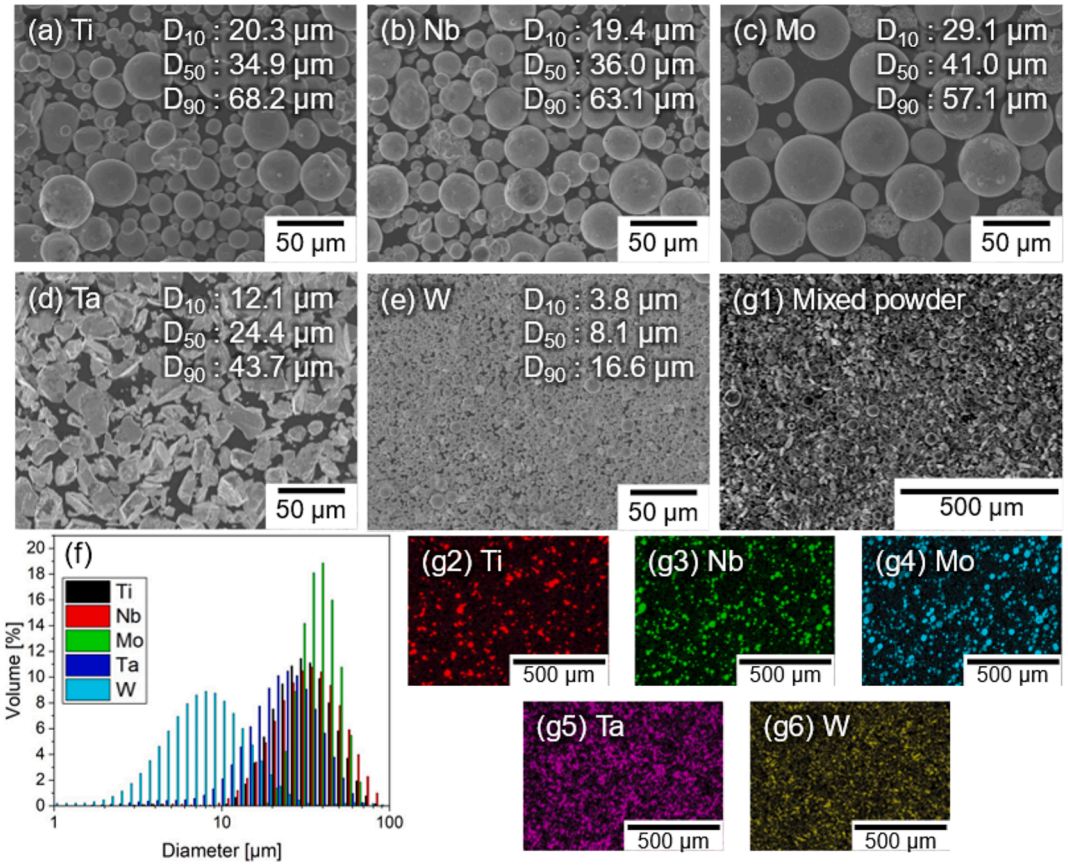

Fig. 3. SEM images of powders: (a) Ti; (b) Nb; (c) Mo; (d) Ta; (e) W; (f) Histogram showing the size distribution of each powder. (g1) Mixed powder and (g2–6) EDS maps of mixed powder corresponding to SEM images.

material yield performance [74].

Fig. 4 shows the OM observation results of the cross sections obtained using different scan strategies and process parameters. For S1000, for which the energy density was the lowest, a relative density of 89.0 % was observed. In contrast, D1000, which involved double XY-scans at the same speed, exhibited an increased relative density (91.9 %) owing to the remelting effect. Remelting is a helpful strategy for securing chemical homogeneity and removing pores by further promoting flow within the melt pool by the Marangoni effect and providing opportunities for mixing unmelted powders [75]. Defects other than unmelted powder or lack of fusion due to insufficient energy input, such as cracking due to residual stress, should be considered for LPBF processing of refractory-based alloys. Moreover, the application of remelting proves effective in eliminating residual stress [76], contributing to the mitigation of crack formation. In the case of S400, when a relatively low scan speed of 400 mm/s was applied, the relative density (92.9 %) increased owing to the increase in the energy density. Higher energy density due to slower scan speeds results in more profound melt pool formation and more prolonged exposure to the laser input. This causes the substrate and surrounding powder to reach a higher overall temperature [77], which results in less unmelted powder. Furthermore, D400, which implemented a double XY-scan at the same speed, exhibited a notably reduced lack of fusion, but vertical solidification cracks along the grain boundaries were detected, resulting in the highest relative density of 98.1 %. These observations revealed the influence of different scanning strategies and process parameters on the relative density of the fabricated structures. However, the realization of industrial-level density (> 99.5 %) for in-situ alloyed HEA necessitates additional research. Nevertheless, the enhancement in density with high-energy density and rescanning approaches showed promising results.

Fig. 5 shows the XRD results for each elemental powder and in-situ alloyed sample fabricated using LPBF. All the in-situ alloyed HEAs showed a single BCC phase, indicating the success of the alloy design with a small ΔT for the LPBF process. The numerical values of 2θ, full width at half maximum (FWHM), and lattice constants (a) for the main (1 1 0) peak of the in-situ alloyed HEA under various process parameters, calculated from XRD measurements, are shown in Supp. Table S4. Notably, peaks of the unmelted powder were observed for S1000 and D1000. However, in the case of S400 and D400, only the BCC peak was detected, and the peaks corresponding to each element powder were not observed. This result indicates the success of uniform melting and the effectiveness of in-situ alloying. Additionally, for D400, a doublet of the BCC peak was observed, which was attributed to the decomposition of $K\alpha_1$ and $K\alpha_2$ X-rays of the Cu target and not the formation of an additional phase. Moreover, the intensity of the $K\alpha_1$ peak is approximately twice that of the $K\alpha_2$ peak [78,79]. In general, the $K\alpha_1$ and $K\alpha_2$ X-rays have similar wavelengths and were observed as a single peak, similar to the S400, S100, and D1000 samples. This phenomenon can be attributed to the narrow peak width of D400, with the full width at half maximum (FWHM) reaching 0.154°, as shown in Supp. Table S4. This reduced FWHM was attributed to the uniform chemical composition [80–82] and the presence of larger grain sizes [78,79], both of which agreed with the results observed using EDS (indicating suppression of segregation) and EBSD (indicating grain size enlargement with epitaxial growth). Moreover, the peaks are shifted to higher angles in the order of S1000, D1000, S400, and D400, which signifies a decrease in the lattice constant as listed in Supp. Table S4, emphasizing a higher solid solution. Therefore, the double XY-scan promoted the formation of a solid solution with more uniform melting.

Fig. 6 shows the SEM and EDS mapping images obtained using different process parameters. For the S1000 and D1000 samples (Fig. 6 (c,d)) at high scan speeds, the powders of each element did not achieve uniform melting, leading to segregation. For the S400 sample (Fig. 6 (a)) with a slow scan speed, the energy density increased and showed relatively uniform mixing, even in the single-scan strategy. However, segregation persisted because of unmelted high melting point powders, such as Ta and W, and non-diffused elements at the melt pool boundaries resulting from convection vortices [83,84]. However, when the double scan was applied under the same conditions (Fig. 6 (b)), segregation was effectively suppressed owing to the higher energy density and remelting, resulting in a more uniform elemental distribution. This observation signifies the development of a homogeneous solid solution, as evidenced by the absence of peaks corresponding to unmelted powder and the narrowest FWHM in XRD analysis (Fig. 5). Moreover, in the context of D400, discernible suppression of constituent element segregation was observed in contrast to the same composition sample produced through

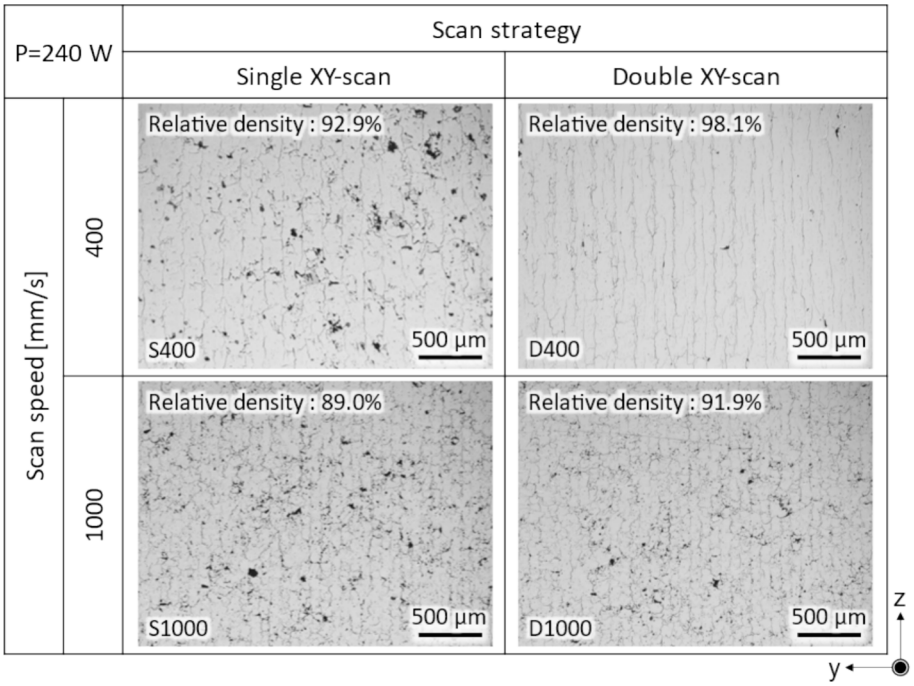

Fig. 4. OM images of cross section for yz-plane fabricated by in-situ alloying with LPBF.

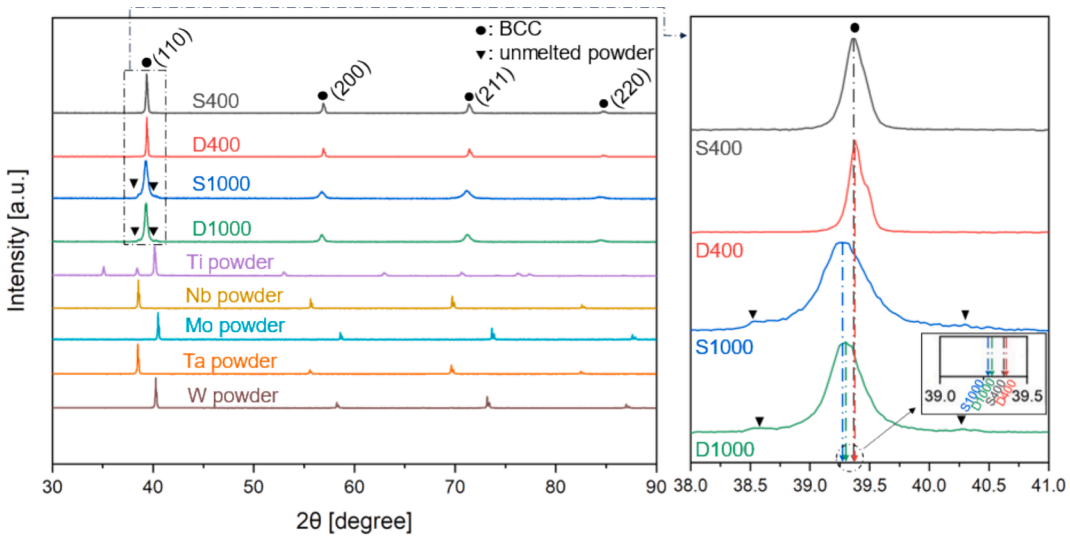

Fig. 5. XRD patterns of the $Ti_1(NbMoTa)_2W_{0.5}$ HEA fabricated by LPBF with in-situ alloying and each powder.

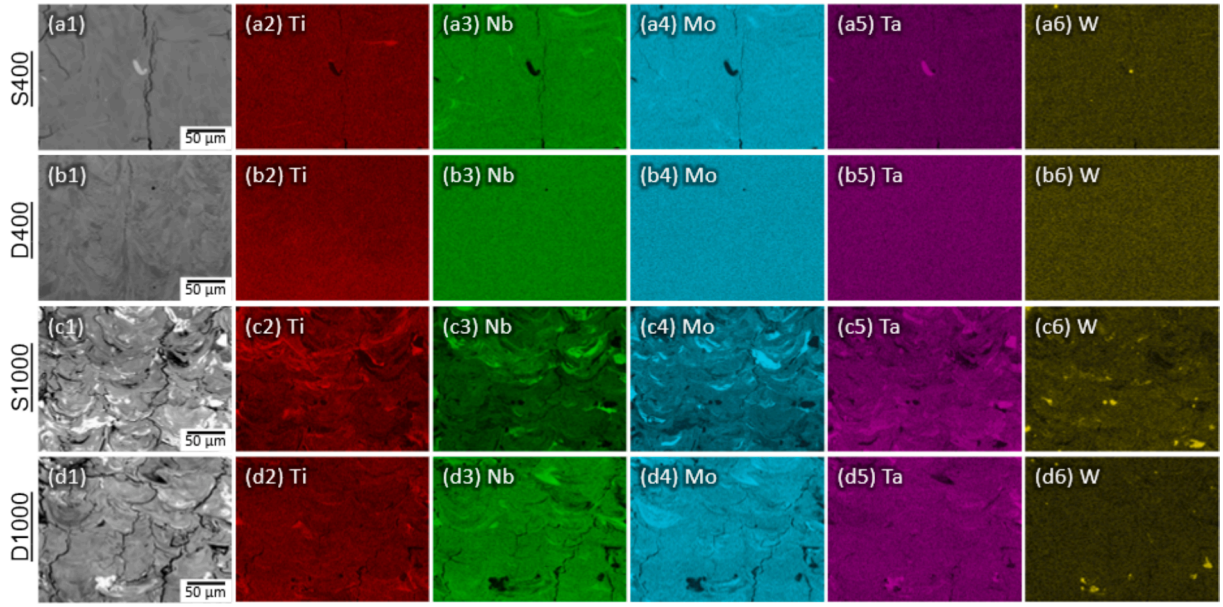

Fig. 6. SEM-BSE image of the (a1) 240 W, 400 mm/s single XY-scan, (b1) 240 W, 400 mm/s, double XY-scan, (c1) 240 W, 1000 mm/s, single XY-scan, (d1) 240 W, 1000 mm/s, double XY-scan. EDS elemental mapping results: (a2–d2) Ti images, (a3–d3) Nb images, (a4–d4) Mo images, (a5–d5) Ta images, (a6–d6) W images.

arc melting in its as-cast state (Supp. Fig. S6). The use of a fast scan speed generates shallow and irregular melt pools, making it challenging to achieve uniform melting of high melting point powders and an insufficient supply of energy for the diffusion of molten elements. However, a low scan speed with high energy density promotes regular and deeper melt pools. Remelting during the double scan induced fluid flow in the molten pool, called the Marangoni effect, further homogenizing the distribution of elements that were not fully melted during the first scan [75]. In addition, remelting promoted the homogenization of unmelted powder and insufficiently mixed powder because it formed a wider melt pool due to the heat accumulated from the previous melt [85]. Fig. 7 illustrates a diagram based on the average of 10 EDS mapping results as quantitative values listed in Supp. Table S5, revealing the differences between the actual and design compositions of each element. The D400 sample exhibited statistically significant differences ($P < 0.01$, Tukey's test) for all elements compared to S400, S1000, and D1000 considering the compositional homogeneity, except for W in the S400 sample. These findings affirm the effectiveness of segregation suppression achieved by a double scan at a high energy density (D400).

Figs. 8 and 9 show the STEM-EDS analyses results conducted on the melt pool boundary and center of the D400 sample, which exhibited the most uniform chemical composition as measured through SEM-EDS measurements. The analyses revealed the formation of a Ti-rich phase at the grain boundaries and interdendritic regions, both at the melt pool boundary and the center (Fig. 8 (a, b), 9 (a, b)). This phase, which exists at the nanoscale, is challenging to observe using XRD and SEM-EDS. Notably, the melt pool boundary exhibited a larger Ti-rich phase and grain size, which was attributed to the slower cooling rate, relative to the center of the melt pool (Fig. 8 (a) and 9 (a)) [86–89]. Furthermore, under relatively slow cooling rates, dendritic (light gray) and interdendritic (dark gray) regions developed within the grains. Nanoscale segregation was observed, with high melting point elements concentrated in the dendritic region and low melting point elements concentrated in the interdendritic region of the melt-pool boundary (Fig. 8

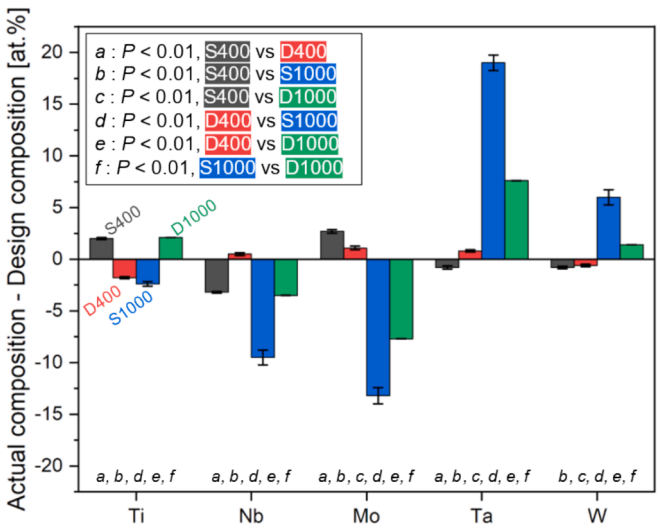

Fig. 7. Distribution of constituent elements of in-situ alloyed $Ti_1(NbMoTa)_2W_{0.5}$ HEA in different process parameter by EDS measurements at Supp. Table S5.

(c2)). Conversely, at the center of the melt pool, where the cooling rate was relatively higher than that at the melt-pool boundary, the interior of the grain demonstrated a more uniform chemical composition (Fig. 9 (c2)). The selected area electron diffraction (SAED) pattern inside the grain of the melt pool center confirmed the BCC structure. Furthermore, the intensity profile analysis revealed the absence of additional diffraction, indicating the absence of intermetallic compounds, such as the B2 phase (Fig. 9 (d1)).

Comprehensive analysis of the Ti-rich phase was performed using high-resolution TEM. The Ti-rich phase exhibited an HCP structure based on a fast Fourier transform (FFT) pattern. Furthermore, the orientation relationship between the matrix and Ti-rich HCP phase was determined to be $[111]_{BCC}//[0001]_{HCP}$ (Fig. 9 (d2)). A similar phenomenon for Ti nanoparticles in this study was reported by other researchers. Zarei et al. explained that Ti and Zr in the HCP structure are easy to separate from Nb, Mo, and Ta in the BCC structure owing to differences in the crystallographic structure [90]. However, the Ti-rich phase concentration at the grain boundary and interdendritic regions observed in this study is expected to arise from the varying diffusion coefficients (D), as follows:

$$D = D_0 \exp(-Q_D/RT) \tag{2}$$

where D_0, Q_D, R, and T are the intrinsic diffusion constant, activation energy for diffusion, gas constant, and absolute temperature, respectively. Fig. 10 shows the temperature-dependent diffusion coefficients for each element calculated using Eq. (2). The values for each variable were obtained from previous studies [91] and are listed in Table 2. Notably, Ti has a relatively lower melting point and higher diffusion coefficient than Nb, Mo, Ta, and W. It was expected that Ti tended to segregate during the solidification and melting of the subsequent layer, causing a cycling thermal effect and forming a Ti-rich phase at the grain boundary and interdendritic regions (Fig. 8 (c1) and 9 (c1)). It is important to note that this alloy design exhibited slight segregation at the interdendritic region in the as-cast form [9], forming micron size BCC phase, other than the matrix, with Ti, Nb, and Mo segregation. However, the suppressed segregation in this study resulted in better homogeneity in the matrix phase owing to the fast-cooling rate of the LPBF process and small ΔT of the designed alloy but pure Ti nanoparticles were formed at grain boundaries and interdendritic regions due to its low melting point and difference in diffusion coefficient.

Fig. 11 shows the EBSD results for different process parameters,

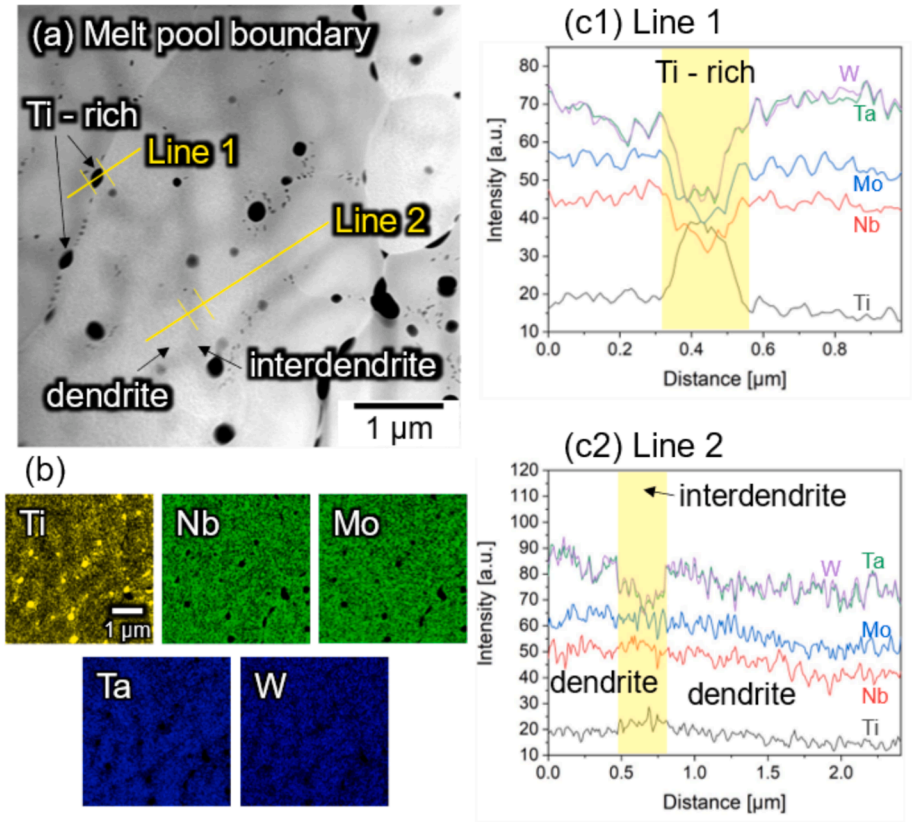

Fig. 8. STEM image from (a1) melt pool boundary of the D400; corresponding elemental distribution maps (b) and line profiles (c1, c2) obtained from STEM-EDS observation.

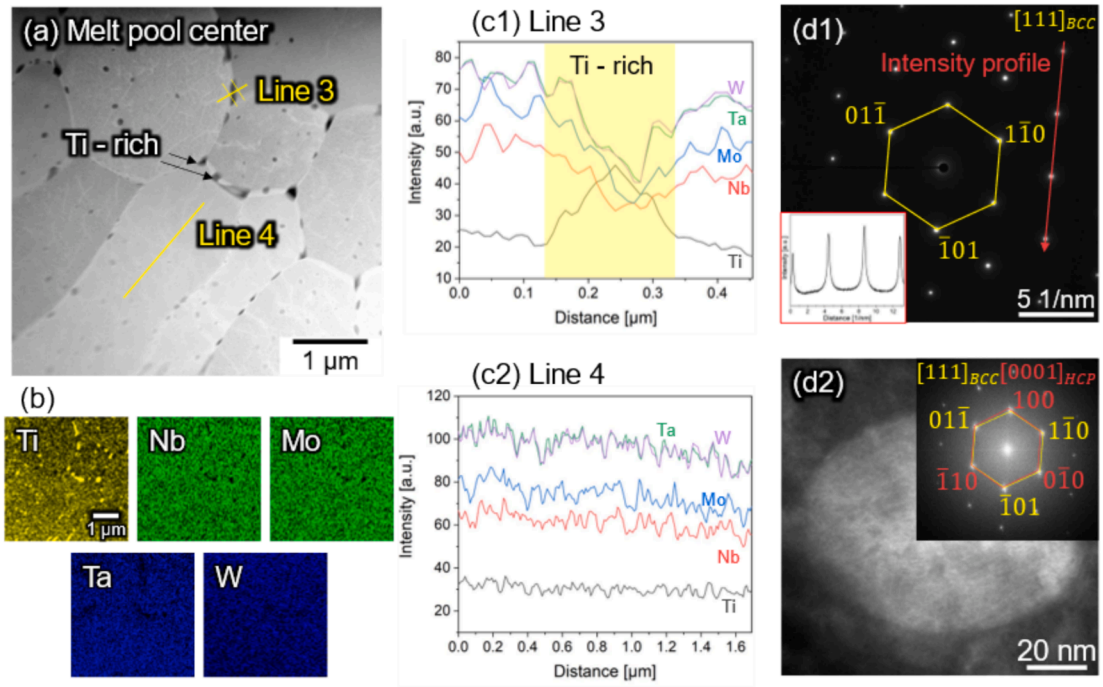

Fig. 9. STEM image from (a1) melt pool center of the D400; corresponding elemental distribution maps (b) and line profiles (c1, c2) obtained by STEM-EDS observation. (d1) SAED patterns inside the grain from the melt pool center. (d2) enlarged Ti-rich phase; corresponding FFT.

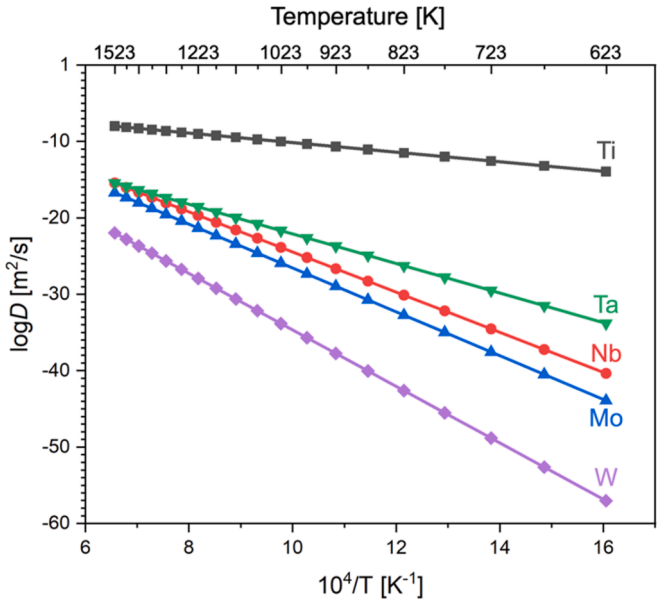

Fig. 10. Self-diffusion coefficients of Ti, Nb, Mo, Ta, and W depending on temperatures.

Table 2
The intrinsic diffusion constant D_0 and activation energy for diffusion Q_D for Ti, Nb, Mo, Ta and W.

	Ti	Nb	Mo	Ta	W
$D_0[10^{-4}m^2s^{-1}]$	1.27E − 4	6.50E + 1	1.39E + 2	1.89E − 3	2.00E + 2
$Q_D[kJ \bullet mole^{-1}]$	119.7	503.0	549.4	370.8	707.7

including the z-direction (building direction, BD) inverse pole figure (IPF) map (Fig. 11 (a1–d1)), {100} pole figure (Fig. 11 (a2–d2)), the high-angle grain boundary (HAGB) map (Fig. 11 (a3–d3)), kernel average misorientation (KAM) maps (Fig. 11 (a4–d4)), and the Taylor factor maps (Fig. 11 (a5–d5)). The KAM map serves as an established metric for residual stress assessment [92,93], derived from the computation of the mean misorientation between individual pixels and their neighboring counterparts. Additionally, the Taylor factor, serving as a geometric gauge, quantifies the efficacy of crystallographic shear mechanisms in accommodating externally imposed macroscopic strains [94]. Random texture was observed for S1000 and D1000 (Fig. 11 (c1–d3)). Consequently, refined grains were formed, which led to an increase in the density of HAGB. High-density HAGB is sensitive to cracking, potentially resulting in a lower relative density [95–97]. For S400, at a reduced scan speed, a relatively uniform melting was achieved with a higher energy density. Consequently, epitaxial growth was achieved in the <100> direction, which is the preferred growth direction for BCC alloys [98]. Moreover, for D400, segregation was effectively suppressed by remelting during the double scan, resulting in strong epitaxial growth and a fiber texture. Moreover, an increase in grain size and a decrease in the density of HAGB was observed compared to S400. In addition, when the energy density increased and remelting was applied, the average misorientation and average Taylor factor decreased.

Fig. 12 shows (a) volumetric energy density, (b) relative density, and EBSD result of (c) Ave. grain size, (d) Density of HAGB. (e) Ave. misorientation and (f) Ave. Taylor factor in Fig. 11. An escalation in relative density was observed concomitant with an increase in VED and the implementation of remelting attributed to a decrease in scan speed, culminating in a maximal relative density of 98.1 % achieved in the D400 configuration, wherein elevated VED and remelting were concurrently applied. Furthermore, a coherent rise in average grain size corresponded to the augmented relative density, indicative of epitaxial growth instigated by heightened VED and remelting. Notably, S1000 and D1000 precluded epitaxial growth due to unmelted powder (Fig. 6 (c,d)). While S400 exhibited a subdued texture alongside remnants of unmelted powder, albeit with segregation partially mitigated through elevated VED, the subsequent application of remelting in D400 engendered a homogeneous solid solution with suppressed segregation, facilitating epitaxial growth across the molten pool and concurrent

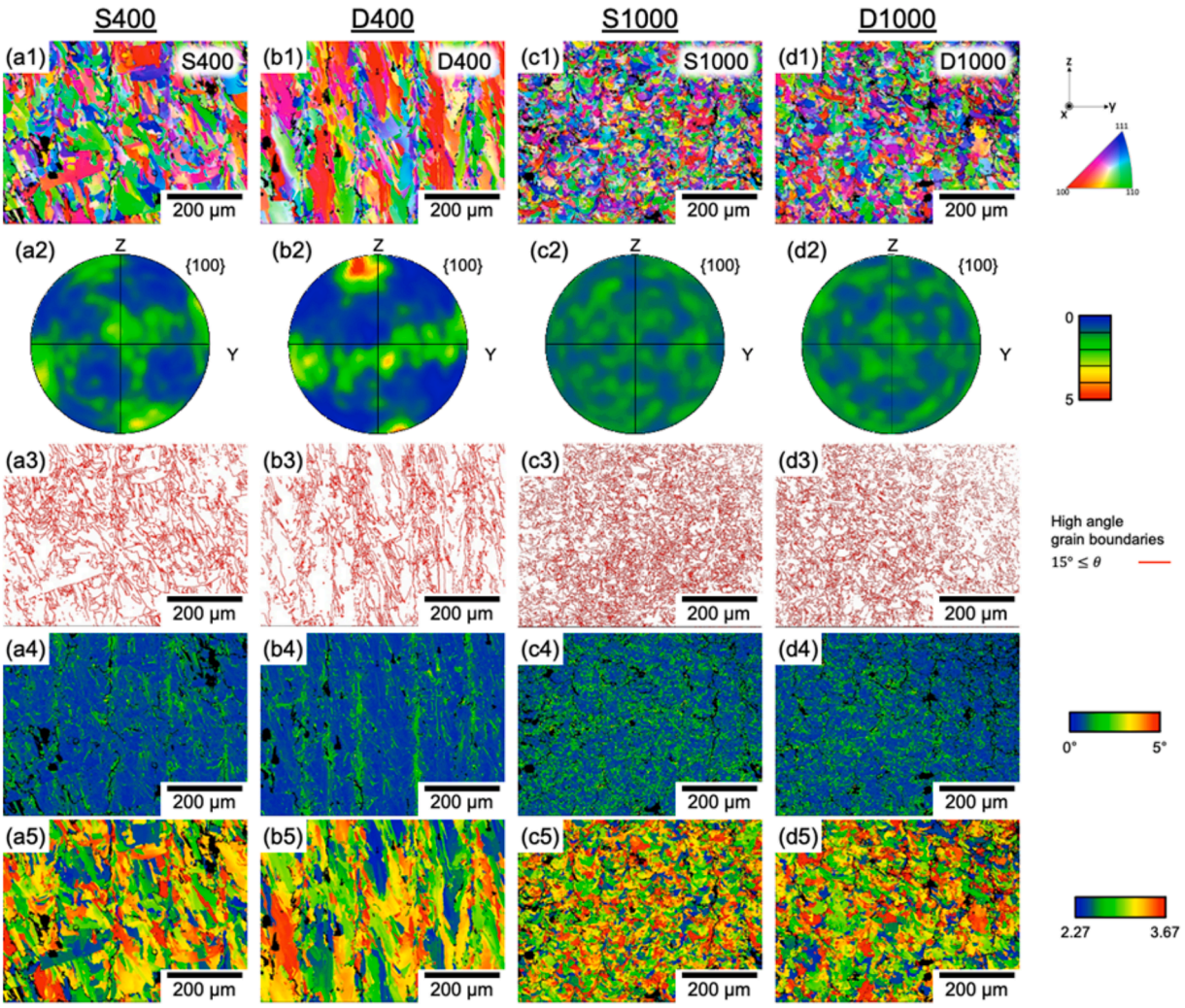

Fig. 11. (a1-d1) The IPF maps along BD and (a2-d2) {100} pole figures of the y-z plane orientation in the Z-direction. (a3-d3) Corresponding high angle grain boundary maps, (a4-d4) the kernel average misorientation maps, and (a5-d5) the Taylor factor maps.

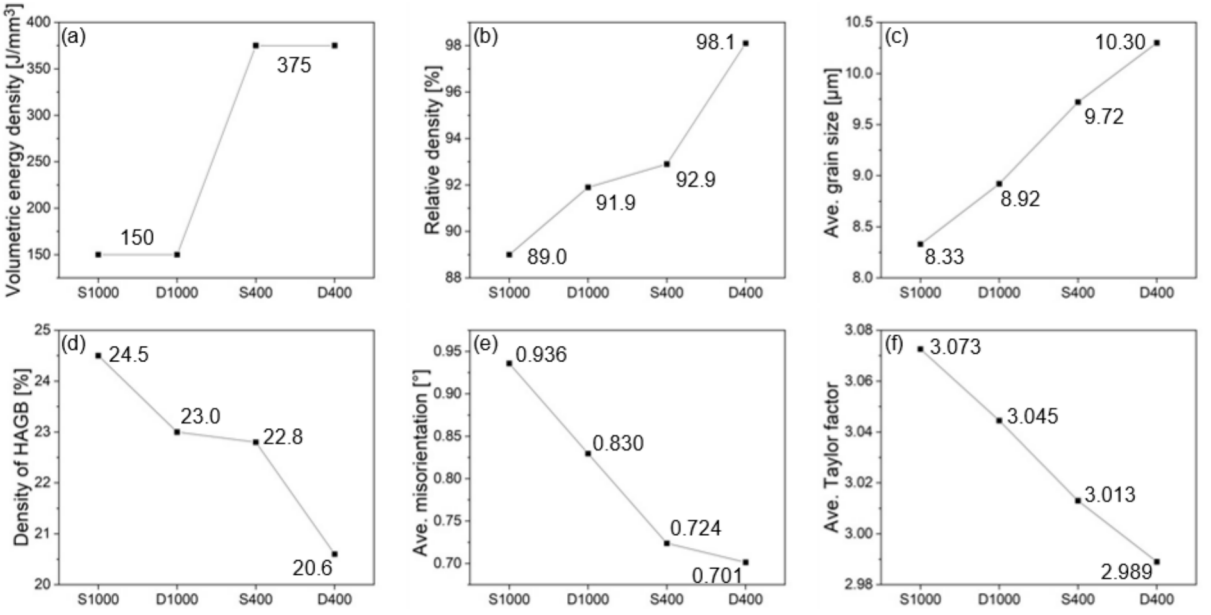

Fig. 12. Plot of (a) Volumetric energy density, (b) Relative density, (c) Ave. grain size, (d) Density of HAGB, (e) Ave. misorientation and (f) Ave. Taylor factor from S1000, D1000, S400, and D400.

augmentation of crystallographic texture. Remelting plays a pivotal role in fostering the development of crystallographic texture [85,99]. Remelting affects the temperature gradient, which is essential for texture formation, and the temperature gradient increases due to heat accumulation from previous melting, thus decreasing the cooling rate. The heightened temperature gradient, attributed to the accumulated heat from prior melting processes [85], actively stimulates epitaxial growth, resulting in a more pronounced crystallographic texture. Texture formation by epitaxial growth decreases the density of HAGB, which is a prominent factor in crack formation. In other words, the suppression of segregation of constituent elements by alloy design with small ΔT, high energy density, and remelting by double scan enabled epitaxial growth, which made it possible to control the crystallographic texture and reduce the density of HAGB (Fig. 12). Furthermore, the augmentation of VED increased the Marangoni force, fostering the uniform dispersion of elements [100]. This phenomenon facilitated the mitigation of constituent element segregation, thereby reducing residual stresses pervading the specimen [101,102]. Additionally, remelting facilitated the fusion and amalgamation of unmelted powder, further diminishing residual stresses. Concurrently, the averaging of constituent elements was curtailed, enabling uniform deformation and consequent reduction in the Taylor factor, indicating enhanced deformation accommodation. Thus, the increase and subsequent remelting of VED suppressed component segregation and elevated relative density by mitigating HAGB and residual stresses—primary contributors to cracks in LPBF—and enhanced deformation accommodation.

Fig. 13 shows the SEM image of the y-z plane for the texture formation mechanism at low magnification (a1–d1), along with the SEM and EBSD images of the magnified region. For S1000, a high scan speed and single scan resulted in inadequate melting and irregular melt pools. Furthermore, epitaxial growth across the melt pool was impeded by undissolved elements at the melt pool boundary. Similarly, D1000 also experiences difficulties in epitaxial growth owing to the unmelted powders. Conversely, S400 and D400, with reduced scan speeds, achieved relatively uniform melting with sufficient energy density, leading to the development of <100> and fiber textures by epitaxial growth in the <100> direction, which is the preferred growth direction for BCC alloys. In both samples, the formation of columnar dendrites was observed around the melt pool boundary, exhibiting a coarser microstructure than the interior of the melt pool. This phenomenon could be

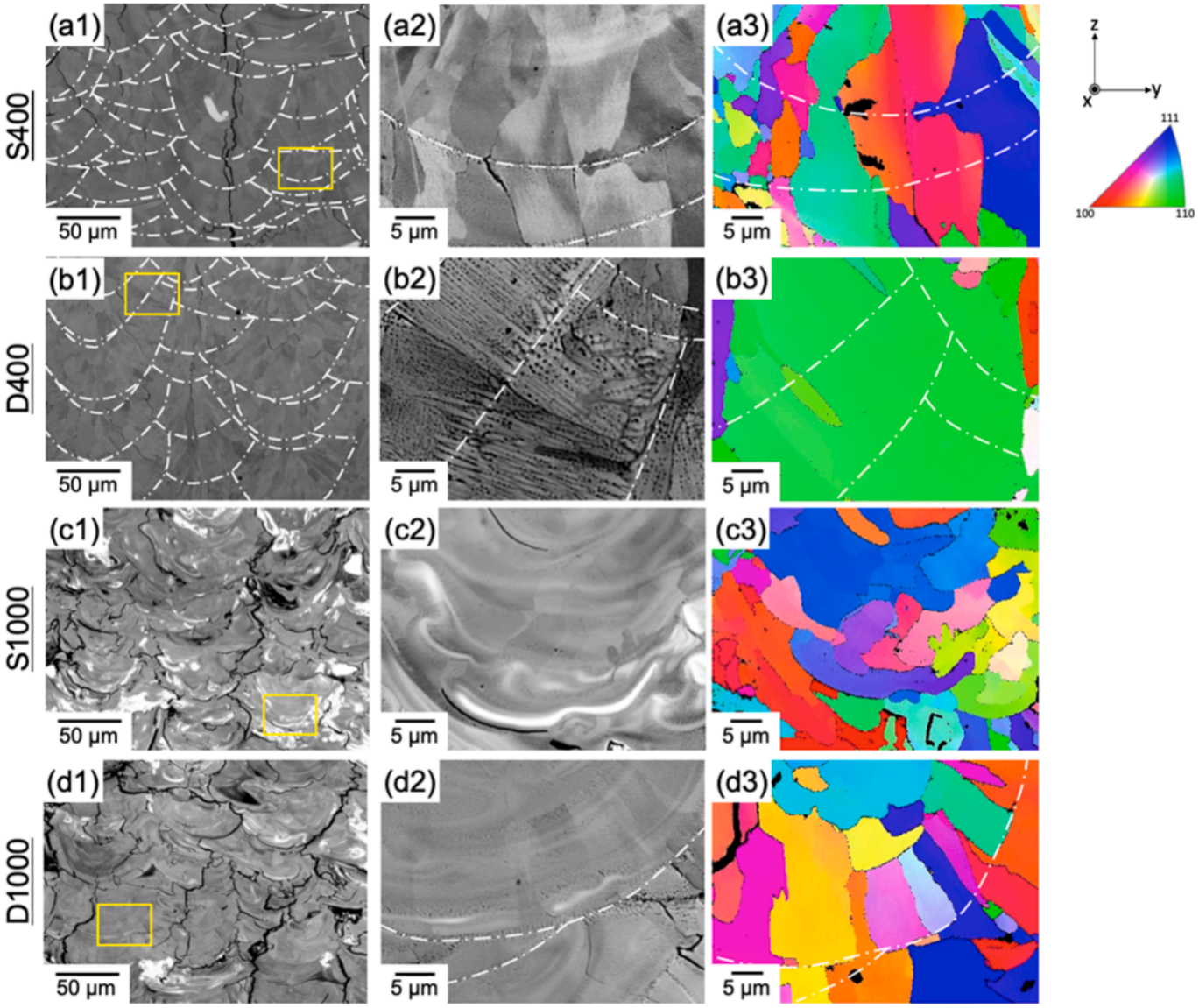

Fig. 13. (a1–d1) SEM-BSE image of the y–z plane showing the melt pool morphology, (a2–d2) magnified images of the areas enclosed in yellow squares in (a1–d1). (a3–d3) Corresponding IPF maps along BD. (For interpretation of the references to colour in this figure legend, the reader is referred to the web version of this article.)

attributed to significant differences in the thermal gradient-to-solidification rate (G/R) and cooling rate (G^*R) at the melt pool boundary [86–89]. Nonetheless, the texture of S400 was relatively weak, presumably because of the obstruction of epitaxial growth caused by a minor proportion of segregation and the unmelted powder. For D400 with a double scan, a columnar microstructure crossing the melt pool was observed in a broader range than that of S400 owing to the increased G caused by the increased heat input of the remelting during double scan resulting in larger and deeper melt pool [85]. Additionally, the difference in the curvatures of the melt-pool boundary resulted in twisted <100> growth, forming a fiber texture [103,104].

Fig. 14 presents the SEM-BSE image capturing the periphery of a crack alongside the corresponding EDS mapping image, KAM map, and HAGB images. In the S1000 configuration, prominent segregation of constituent elements is evident, primarily attributed to the disparate melting points of elements. Insufficient melting leads to the existence of liquid metal in localized areas, thereby engendering tensile stress/strain stemming from solidification and thermal shrinkage, mainly concentrated around the liquid film region [101,102]. Solidification cracking ensues when localized tensile stress/strain surpasses the material's resistance to fracture, a phenomenon corroborated by the concentration of residual stress proximal to the crack initiation site as evidenced by the KAM map. Moreover, crack propagation along HAGB, which is inherently susceptible to propagation, further validates this observation. Conversely, in the D400 configuration, segregation of constituent elements is notably absent around the crack periphery, resulting in a diminished distribution of residual stress. Consequently, transverse crack formation, prevalent in the S1000 scenario, is mitigated. Here, HAGB emerges as the principal precursor to crack formation [95–97]. Thus, residual stress and HAGB reduction are paramount in curtailing crack propagation and bolstering the relative density of in-situ alloyed HEAs. For instance, strategies to achieve precise texture control to minimize high-angle grain boundaries (HAGB), which are key factors influencing crack initiation, have significant potential [96,105]. Furthermore, reducing the residual stresses through elevated preheating temperatures [106,107] and optimizing smaller scan lengths [108,109] are avenues for further investigation.

Fig. 15 illustrates the microstructure formation and crack propagation mechanism for the in-situ alloyed HEA while considering dendritic growth orientation, the existence of unmelted powder after the first scan, nano Ti-phase formation, and crack prevention with texture strengthening after rescan. The matrix of the BCC structure preferentially grows in the <100> direction along the G perpendicular to the boundary of the melt pool [110], as indicated with dendritic growth with rotated BCC during solidification, thus, resulting randomly oriented grains (random texture). Subsequently, Ti, characterized by its low melting point and rapid diffusion rate, diffused owing to the repeated heat input from the LPBF. The Ti-rich phase accumulates at the grain boundaries or interdendritic regions with a small critical energy for nucleation. At the melt pool boundary, a larger Ti-rich phase was observed because the cooling rate was lower than at the melt pool center [111]. Therefore, epitaxial growth across the melt pool was feasible

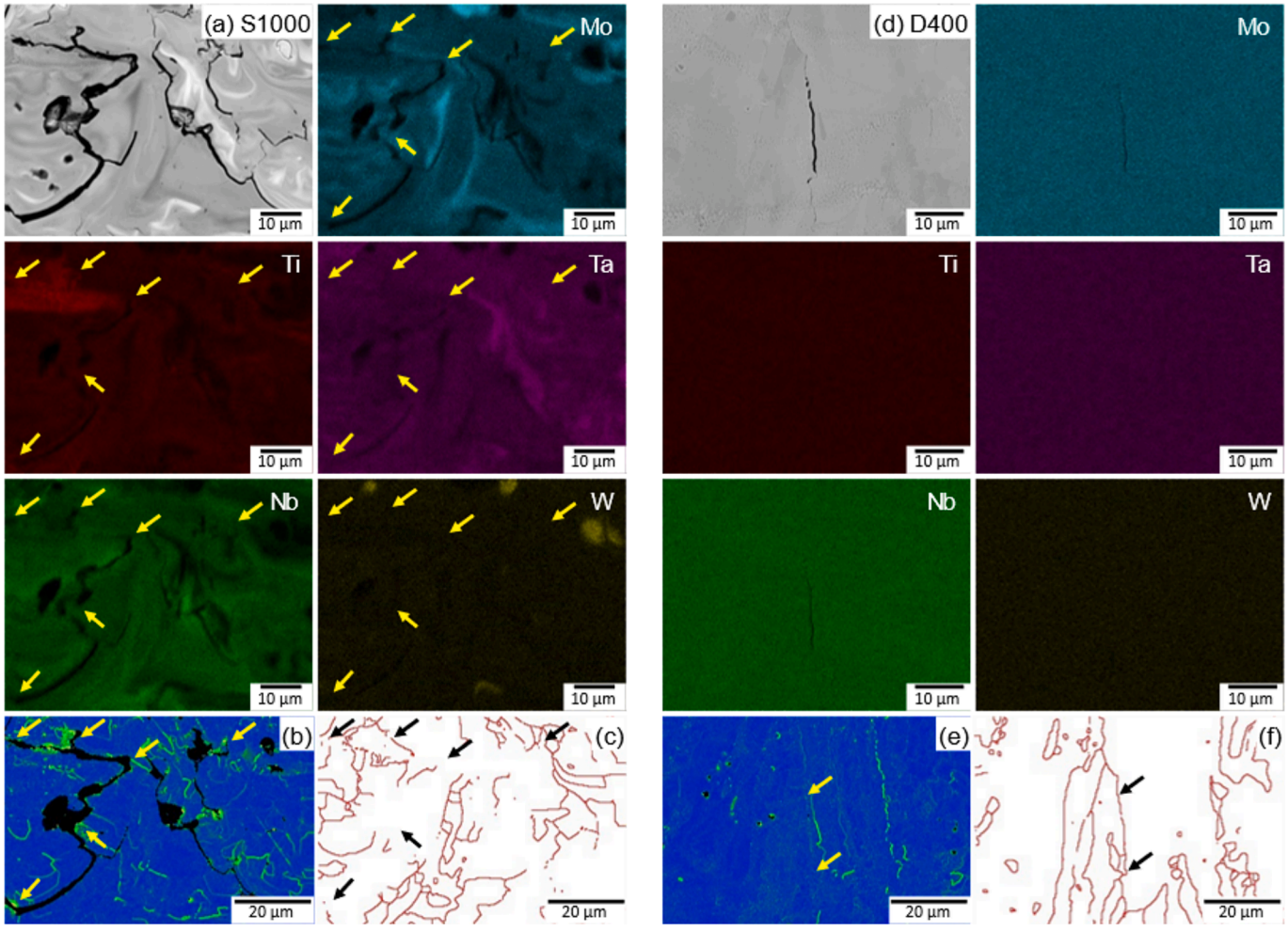

Fig. 14. SEM-BSE image and EDS mapping result of the (a) S1000, (b) D400 samples around crack. Corresponding (b,e) the kernel average misorientation maps, and (c,f) high angle grain boundary maps by EBSD.

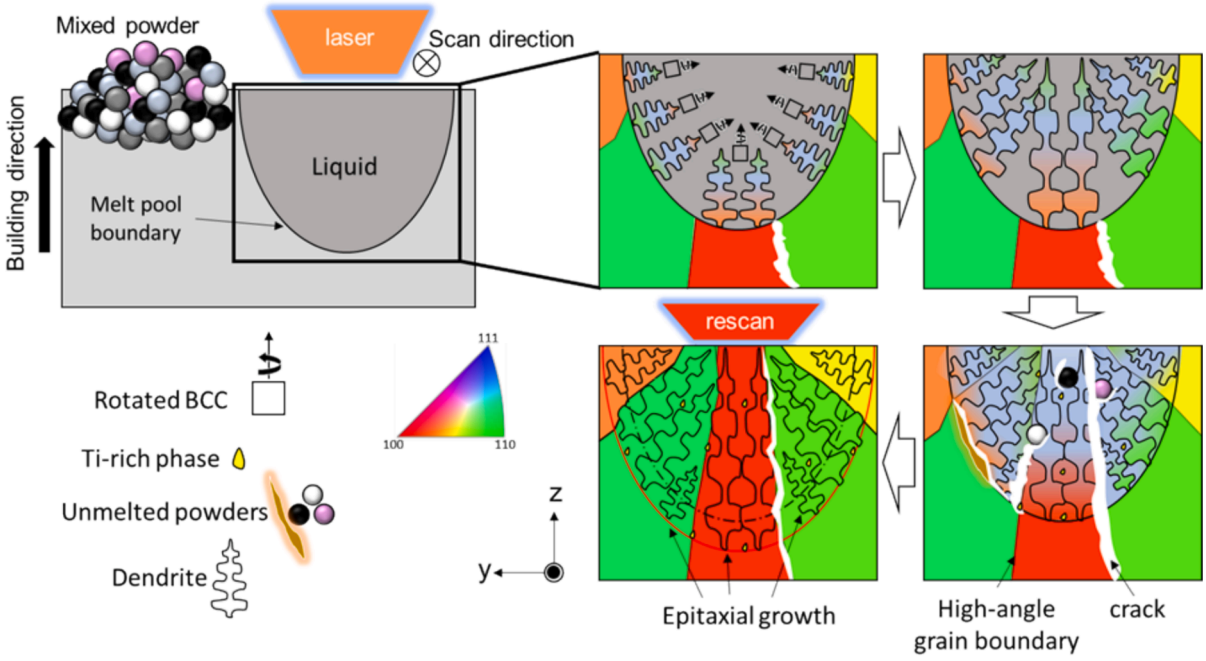

Fig. 15. Schematic representation of the solidification mechanism for the texture formation for in-situ alloyed HEA.

because the formation of a Ti-rich phase was achieved after the BCC matrix growth. The presence of unmelted powder hinders epitaxial growth. Nevertheless, remelting (rescan) induces a broader and deeper melt pool facilitated by the accumulated heat from preceding melting cycles [85]. The broader and deeper melt pool eliminates residual unmelted powder and alleviates residual stresses [76]. Furthermore, the augmented temperature gradient from the accumulated heat by remelting actively fosters epitaxial growth [85,99]. Consequently, crystallographic texture formation was achieved despite the presence of Ti-rich compounds. However, the misalignment of dendrite growth at the melt pool center and side branches leads to the formation of HAGB in the center of the melt pool [59]. The ensuing crack propagates along the HAGB parallel to the BD, as shown in Fig. 4.

Fig. 16 shows the nanohardness results for different process parameters to assess the success of solid solution strengthening by suppressed segregation. Fig. 16 (a) shows the representative load–displacement curves (p–h curves) for each condition. It is evident that the maximum indentation depth decreases, and the slope of the loading stage increases in the sequence of S1000, D1000, S400, and D400. This trend indicates that the D400 sample exhibited the highest hardness and was less prone to deformation. The observed strengthening effect was attributed to solid-solution strengthening, which was achieved by suppressing segregation through alloy design with small ΔT, high-energy density and remelting in the double scan process. Fig. 16 (b) shows the average nano-hardness from ten indentations for each condition. The nano-hardness values under each condition exhibited statistically significant differences (** $P < 0.01$, Tukey's test). The S1000 sample exhibited the most extensive error bar, with the error bar size decreasing in the order D1000 > S400 > D400. These results are associated with the suppression of the segregation and an increase in densification owing to double scan and/ or increase in VED with scan speed control. The segregation part of the constituent elements had lower nanohardness than the homogeneous elemental distribution part due to the decrease in the solid solution strengthening (Supp. Fig. S8). In addition, the area around the crack showed relatively lower nanohardness than the area without cracks. These results are consistent with the nanohardness trend in Fig. 16. That is, the existence of more cracks resulted in lower relative density and lower nanohardness (S1000), and higher nanohardness was achieved when the densification increased owing to the decrease in cracks (D400). Also, these results align with the SEM-EDS observations in Fig. 6

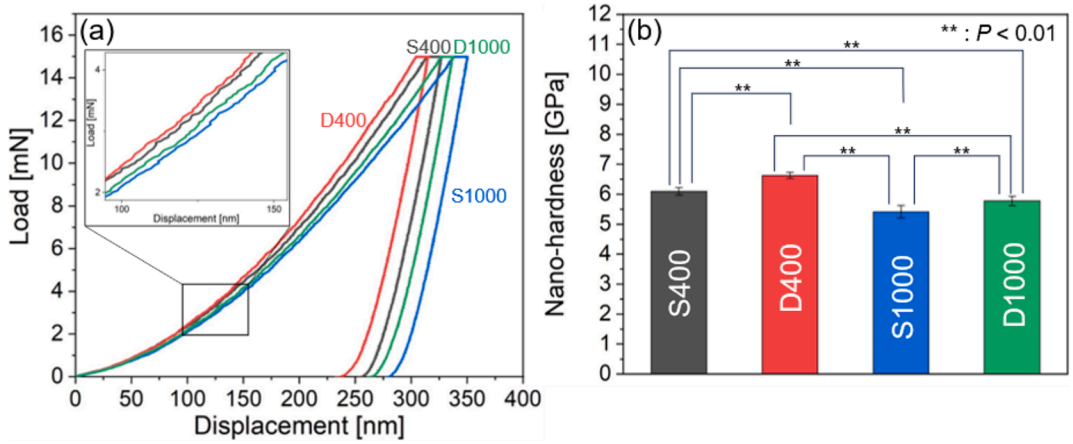

Fig. 16. (a) Representative nanoindentation load–displacement curves of in-situ HEAs. (b) Nano-hardness of in-situ HEAs in the average of 10 times measurement.

and reinforce the advantages of the double scan method for achieving remelting and improving mechanical properties.

Fig. 17 presents the mechanical properties derived from the compression test of in-situ alloyed HEA (D400) and previously reported as-cast HEA [9] alongside SUS316L and CP-Ti, conventional biomaterials chosen for comparison. The compression test for D400 was conducted parallel to the y-axis to mitigate the effect of the crack propagated along the BD. The stress–strain curve is shown in Supp. Fig. S7. The in-situ alloyed HEA exhibited noteworthy yield stress of 1205.8 MPa (Supp. Table S6), surpassing conventional biomaterials of SUS316L (320.0 MPa) [112] and CP-Ti (393.0 MPa) [113]. This enhancement is attributed to solid solution strengthening facilitated by forming a homogeneous solid solution with suppressed segregation. D400 showed higher strength than as-cast HEA, which is attributed to the Hall-Petch effect due to small grain size [114,115]. Furthermore, Young's modulus of D400 measured at 135.5 GPa was lower than SUS316L (187.0 GPa) [112] and slightly higher than CP-Ti (104.0 GPa) [113]. Given the reported issues of stress shielding arising from differences in Young's modulus relative to natural human bone (~30 GPa) [116–120], strategies such as porous materials [121,122] and crystallographic texture control [28,123,124] have been proposed for Young's modulus reduction. The reduced Young's modulus of D400 was achieved by <100> texture development owing to its less stiff atomic arrangement compared to other crystal orientations. Consequently, a subsequent study will delve into the reduction of Young's modulus through further crystallographic texture control. Moreover, mechanical anisotropy is an important aspect of additively manufactured components regarding texture and defects, thus, the dependence of mechanical properties on fabrication direction will be considered in a future study.

Fig. 18 shows the biocompatibility of the in-situ alloyed HEA (D400) compared to the control groups, including SUS316L stainless steel and CP-Ti, which are widely used as biomaterials. Fig. 18 (a) shows the results of the quantitative analysis of osteoblast density after 24 h of culture, evaluated using Giemsa staining (Fig. 18 (b)). The in-situ alloyed HEA exhibited cell densities similar to those of CP-Ti, with no statistically significant differences between the two samples. Moreover, the cell density was significantly higher than that of SUS316L. Fig. 18 (c) shows fluorescent images of the cytoskeletal components and focal adhesion of osteoblasts adhered to the samples. The morphology of osteoblasts on biomaterials is a crucial factor, along with the cell density. In SUS316L cells, osteoblasts appeared to be reduced in size owing to poor cytoskeletal organization. In contrast, both CP-Ti and in-situ alloyed HEA exhibited extensive morphology with a dense network of actin fibers. The same trend was observed for the Giemsa-stained samples, as shown in Fig. 18 (b). Considering that the segregation caused inhibition in cell spreading, the homogeneity in cell density and cell spreading on in-situ alloyed HEA highlighted the importance of suppressed segregation in this study. The in-situ alloyed HEA of the Ti-Nb-Mo-Ta-W combination demonstrated good biocompatibility comparable to that of CP-Ti.

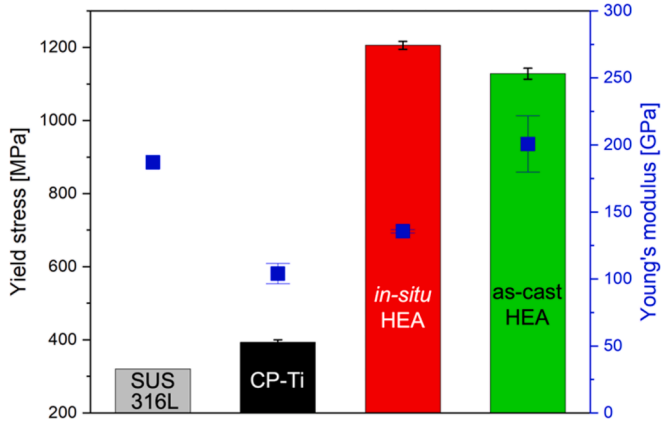

Fig. 17. Comparison of Yield stress and Young's modulus of in-situ HEA (D400) by compression test with SUS316L and CP-Ti.

The proposed $Ti_1(NbMoTa)_2W_{0.5}$ alloy processed by LPBF presented promising results, considering suppressed segregation to reduce cracks with microstructure optimization and realized solid solution strengthening to achieve better mechanical properties than commercial alloys and its cast form, which suggested better biocompatibility and corrosion resistance (a planned future study concept). Moreover, the critical stress shielding issue for implant materials due to Young's modulus difference in bone and BioHEAs with superior mechanical strength can be solved by the successful texture formation, as proposed in this study.

4. Limitations and challenges

HEA design strategy with a particular intention for biological applications is called BioHEA mainly composed of elements with good biocompatibility, such as non-toxic and non-allergenic. As refractory elements are bioinert, they are preferred in BioHEA design. However, refractory metals and alloys are difficult to process by LPBF due to their brittle nature under the fast-cooling condition of LPBF, which results in cracks, especially along the HAGBs with high residual stress [125]. Therefore, reaching industrially accepted HEA bulk density is one of the challenges for LPBF processing. The alloy design for high ductility and high preheat temperature application during the LPBF process can be proposed to overcome this limitation.

To evaluate the strength of BioHEA, the tensile and compression performance would be beneficial because the bone is constantly under tension and/ or compression forces. However, the current limitation lies in achieving fully dense refractory BioHEAs due to defects, such as cracking, exhibiting premature fracture under tensile load. The cracking problem during LPBF-processing of refractory metals and alloys is due to the residual stress along the grain boundaries, causing solidification cracks. However, the main reason for solidification crack (residual stress) can be reduced by the simultaneous approach of alloy design with small ΔT, process parameter optimization, and remelting application as proposed in this study to prevent excessive residual stress while enhancing the heat accumulation and thus reduced the cooling rate and consequent decrease in residual stress. This study was the first to report the successful application of in-situ alloying for refractory HEA owing to the alloy design approach, process parameter optimization, remelting implementation, and texture control to enhance sustainability while tuning grain boundary characteristics to prevent crack occurrence, realizing over 98 % density without significant segregation and phase separation, thus resulted in superior mechanical performance. For further enhancement in densification, the high preheat application is suggested to prevent the solidification stress-related cracking phenomenon.

However, the mechanical performance of refractory HEAs under tensile load is still unsatisfying, therefore, alloy design strategies focusing on decreasing valance electron concentration (VEC) to enhance the ductility of HEAs have been investigated [126]. Moreover, it is suggested to investigate the other functionalities of proposed alloy systems, other than tensile performance, such as their corrosion and/ or tribocorrosion properties, particularly in simulated body fluids [127].

Biological performance of HEAs has been a topic of focus for biomedical applications to realize good mechanical performance and cellular behavior. However, compositional variations in Ti-based alloys have been ineffective to enhance cell behavior [128]. Therefore, strategies such as forming surface roughness and coating are critical research topics to improve cell behavior on metal surfaces [129,130]. While the surface roughness can enhance cell attachment, the coating can be applied to enhance cell proliferation and differentiation. With the mentioned approaches, the performance of BioHEA can be enhanced to a certain level, however, the cracking due to the brittle nature of refractory metals remains a major challenge for commercial LPBF machines with limited preheating capabilities. Further development in

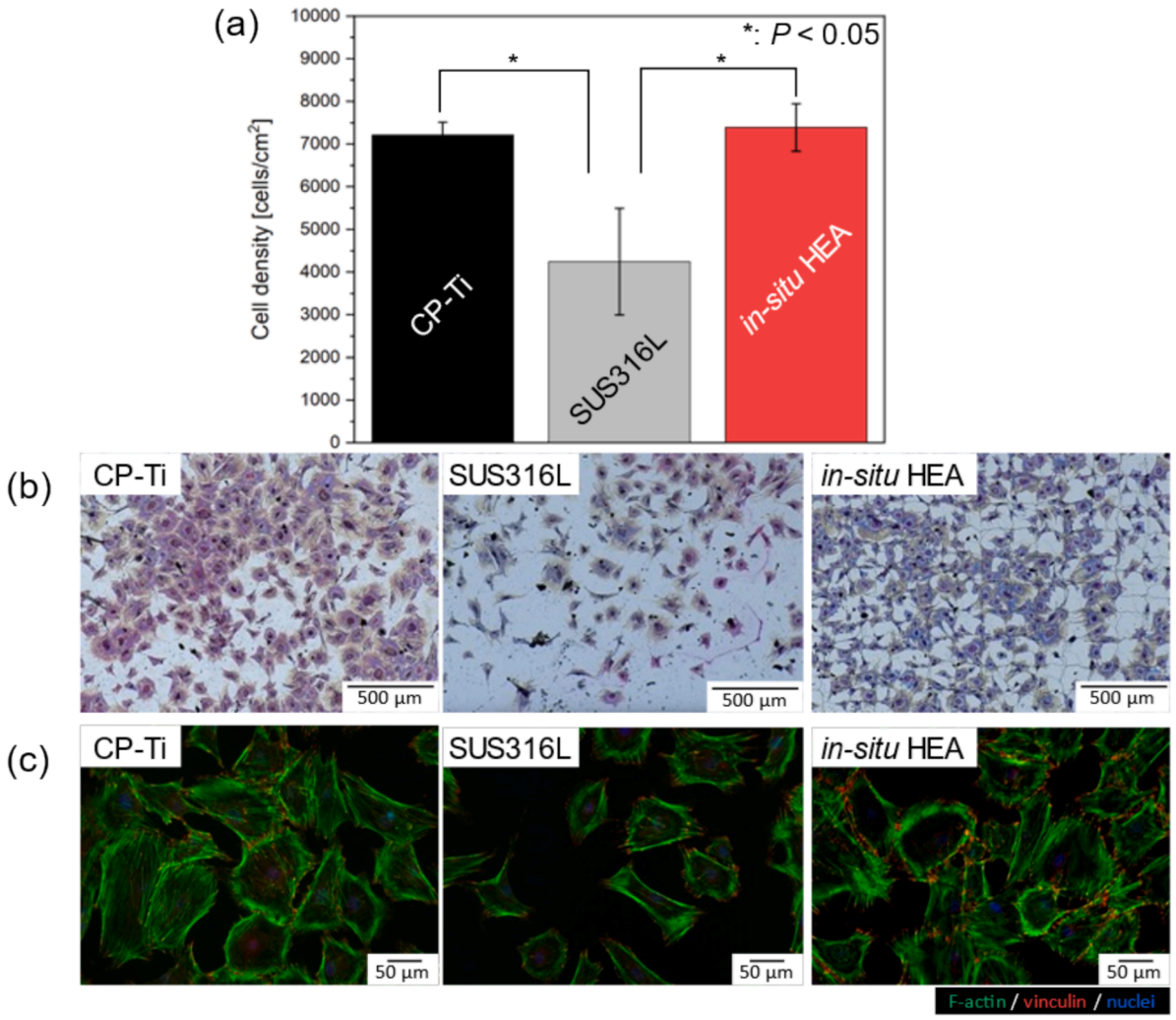

Fig. 18. Biocompatibility of in-situ alloyed $Ti_1(NbMoTa)_2W_{0.5}$ in comparison with CP-Ti, and SUS316L. (a) Quantitative analysis of cell density; *: $P < 0.05$. (b) Giemsa and (c) fluorescent staining images of osteoblasts adhesion on the specimens.

LPBF technology and HEA design is expected to bring new solutions to emerging needs of high-performing BioHEA part design.

5. Conclusion

Non-equiatomic $Ti_1(NbMoTa)_2W_{0.5}$ HEA alloyed in-situ using LPBF was prepared by mixing Ti, Nb, Mo, Ta, and W powders. The following conclusions were drawn from this study:

(1) In XRD, under low-scan speed and double scan conditions, the peak of each powder was not detected, and only a single BCC peak was observed, indicating the formation of a single solid solution by uniform melting via in-situ alloying. In addition, the relative density was highest under the same conditions, and cracking was suppressed.
(2) The segregation of the constituent elements by the unmelted powder was observed at a high scan speed and in a single scan. However, under a slow scan speed and double scan conditions, uniform melting was achieved by increasing the energy density and remelting effect. The segregation of the constituent elements was suppressed at the microlevel; STEM-EDS was observed only on a nanoscale Ti-rich phase. Consequently, the nanohardness increased owing to the solid solution strengthening.
(3) By double scan strategy enhancing the heat accumulation and consequently reducing the residual stress which is the main parameter of solidification crack, larger and deeper melt pool formation was realized, promoting epitaxial growth and forming columnar grain along the BD, which increased the grain size and consequently decreased the HAGB density which are initiation and propagation sites for solidification crack.
(4) At a fast scan speed, epitaxial growth with a low energy density was impossible; therefore, a random texture was formed. However, the larger melt pool caused by remelting removed the unmelted powder, and the increased thermal gradient promoted epitaxial growth. The figure shows the crystallographic texture of <100> and the fiber textures.
(5) The D400 sample obtained by in-situ alloying with LPBF showed higher yield stress than the as-cast one and significantly higher than CP-Ti and excellent biocompatibility, comparable to that of CP-Ti. This result highlights its potential as a metallic biomaterial for new BioHEAs.

This study demonstrated the effectiveness of in-situ alloying by replacing a pre-alloyed powder with a mixed powder. Segregation of the constituent elements was effectively suppressed by optimizing the process parameters, and the crystallographic texture was controlled. Therefore, in-situ alloying with mixed powders is promising for saving time and cost and achieving high design freedom of HEA. In conclusion, LPBF process with fast cooling rate and small ΔT of the BioHEA resulted in single phase with suppressed segregation even with the application of

challenging in-situ alloying of elemental feedstock powders, moreover, proposing the advantage of texture control to enhance its functionality. However, further studies are required to reduce the cracks in the fabrication of high-density samples by in-situ alloying with LPBF for exceptional performance regarding tribocorrosion to consider for biological applications.

CRediT authorship contribution statement

Yong Seong Kim: Writing – original draft, Visualization, Methodology, Investigation, Formal analysis, Data curation. **Ozkan Gokcekaya:** Writing – review & editing, Validation, Supervision, Methodology, Funding acquisition, Conceptualization. **Kazuhisa Sato:** Writing – review & editing, Methodology, Investigation. **Ryosuke Ozasa:** Writing – review & editing, Project administration. **Aira Matsugaki:** Writing – review & editing, Methodology, Investigation. **Takayoshi Nakano:** Writing – review & editing, Supervision, Resources, Funding acquisition, Conceptualization.

Declaration of competing interest

The authors declare that they have no known competing financial interests or personal relationships that could have appeared to influence the work reported in this paper.

Acknowledgment

This work was supported by a Grant-in-Aid for Scientific Research (JP23H00235 and JP24K07254) from the Japan Society for the Promotion of Science (JSPS) and CREST-Nanomechanics: Elucidation of macroscale mechanical properties based on understanding the nanoscale dynamics of innovative mechanical materials (Grant Number: JPMJCR2194) from the Japan Science and Technology Agency (JST).

Appendix A. Supplementary data

Supplementary data to this article can be found online at https://doi.org/10.1016/j.matdes.2025.113824.

Data availability

Data will be made available on request.

References

[1] B. Cantor, I. Chang, P. Knight, A. Vincent, Microstructural development in equiatomic multicomponent alloys, Mater. Sci. Eng. A 375 (2004) 213–218, https://doi.org/10.1016/j.msea.2003.10.257.
[2] J.W. Yeh, S.K. Chen, S.J. Lin, J.Y. Gan, T.S. Chin, T.T. Shun, C.H. Tsau, S. Y. Chang, Nanostructured high-entropy alloys with multiple principal elements: novel alloy design concepts and outcomes, Adv. Eng. Mater. 6 (5) (2004) 299–303, https://doi.org/10.1002/adem.200300567.
[3] Y. Ye, Q. Wang, J. Lu, C. Liu, Y. Yang, High-entropy alloy: challenges and prospects, Mater. Today 19 (6) (2016) 349–362, https://doi.org/10.1016/j.mattod.2015.11.026.
[4] D.B. Miracle, O.N. Senkov, A critical review of high entropy alloys and related concepts, Acta Mater. 122 (2017) 448–511, https://doi.org/10.1016/j.actamat.2016.08.081.
[5] B. Cantor, Multicomponent high-entropy Cantor alloys, Prog. Mater. Sci. 120 (2021) 100754, https://doi.org/10.1016/j.pmatsci.2020.100754.
[6] A. Motallebzadeh, N.S. Peighambardoust, S. Sheikh, H. Murakami, S. Guo, D. Canadinc, Microstructural, mechanical and electrochemical characterization of TiZrTaHfNb and Ti1. 5ZrTa0. 5Hf0. 5Nb0. 5 refractory high-entropy alloys for biomedical applications, Intermetallics 113 (2019) 106572. https://doi.org/10.1016/j.intermet.2019.106572.
[7] G. Perumal, H.S. Grewal, M. Pole, L.V.K. Reddy, S. Mukherjee, H. Singh, G. Manivasagam, H.S. Arora, Enhanced biocorrosion resistance and cellular response of a dual-phase high entropy alloy through reduced elemental heterogeneity, ACS Appl. Bio Mater. 3 (2) (2020) 1233–1244, https://doi.org/10.1021/acsabm.9b01127.
[8] T. Nagase, M. Todai, T. Hori, T. Nakano, Microstructure of equiatomic and non-equiatomic Ti-Nb-Ta-Zr-Mo high-entropy alloys for metallic biomaterials, J. Alloy. Compd. 753 (2018) 412–421, https://doi.org/10.1016/j.jallcom.2018.04.082.
[9] Y.S. Kim, R. Ozasa, K. Sato, O. Gokcekaya, T. Nakano, Design and development of a novel non-equiatomic Ti-Nb-Mo-Ta-W refractory high entropy alloy with a single-phase body-centered cubic structure, Scr. Mater. 252 (2024) 116260, https://doi.org/10.1016/j.scriptamat.2024.116260.
[10] T. Matsuzaka, A. Hyakubu, Y.S. Kim, A. Matsugaki, T. Nagase, T. Ishimoto, R. Ozasa, H.S. Kim, T. Mizuguchi, O. Gokcekaya, Development of an equiatomic octonary TiNbTaZrMoHfWCr super-high-entropy alloy for biomedical applications, Mater. Chem. Phys. (2024) 129120, https://doi.org/10.1016/j.matchemphys.2024.129120.
[11] D. Lin, J. Hu, M. Liu, Z. Li, X. Xi, J. Dai, R. Ma, Z. Shi, C. Tan, R. Li, Enhancing plasticity in laser additive manufactured high-entropy alloys: The combined effect of thermal cycle induced dissolution and twinning, Addit. Manuf. 93 (2024) 104427, https://doi.org/10.1016/j.addma.2024.104427.
[12] Z. Han, C. Guo, C. Huang, X. Fan, J. Zhang, G. Liu, H. Wang, R. Wei, Corrosion resistant body-centered cubic VNbTa refractory medium-entropy alloy, Corrosion Sci. 229 (2024) 111885, https://doi.org/10.1016/j.corsci.2024.111885.
[13] H. Ozdemir, A. Nazarahari, B. Yilmaz, U. Unal, H. Maier, D. Canadinc, E. Bedir, R. Yilmaz, Understanding the enhanced corrosion performance of two novel Ti-based biomedical high entropy alloys, J. Alloy. Compd. 956 (2023) 170343, https://doi.org/10.1016/j.jallcom.2023.170343.
[14] H. Li, X. Li, C. Jin, Q. Li, Q. Ma, K. Hua, H. Wang, W. Liu, Mechanical and tribological performance of AlCr0. 5NbTaxTi4–x (x= 0, 0.5, 1) refractory high-entropy alloys, Journal of Materials Science & Technology 156 (2023) 241-253. https://doi.org/10.1016/j.jmst.2023.02.016.
[15] B. Chen, X. Li, W. Chen, L. Shang, L. Jia, Microstructural evolution, mechanical and wear properties, and corrosion resistance of as-cast CrFeNbTiMox Refractory high entropy alloys, Intermetallics 155 (2023) 107829, https://doi.org/10.1016/j.intermet.2023.107829.
[16] A. Chavan, S. Mandal, M. Roy, Cobalt free refractory high entropy alloys for total joint arthroplasty: In-vitro wear, corrosion and cytocompatibility evaluation, J. Alloy. Compd. 938 (2023) 168499, https://doi.org/10.1016/j.jallcom.2022.168499.
[17] P. Kumar, N.K. Jain, S. Jaiswal, S. Gupta, Development of Ti–Ta–Nb–Mo–Zr high entropy alloy by μ-plasma arc additive manufacturing process for knee implant applications and its biocompatibility evaluation, J. Mater. Res. Technol. 22 (2023) 541–555, https://doi.org/10.1016/j.jmrt.2022.11.167.
[18] M. Todai, T. Nagase, T. Hori, A. Matsugaki, A. Sekita, T. Nakano, Novel TiNbTaZrMo high-entropy alloys for metallic biomaterials, Scr. Mater. 129 (2017) 65–68, https://doi.org/10.1016/j.scriptamat.2016.10.028.
[19] M. Wang, Z. Ma, Z. Xu, X. Cheng, Microstructures and mechanical properties of HfNbTaTiZrW and HfNbTaTiZrMoW refractory high-entropy alloys, J. Alloy. Compd. 803 (2019) 778–785, https://doi.org/10.1016/j.jallcom.2019.06.138.
[20] L. Fang, J. Wang, X. Li, X. Tao, Y. Ouyang, Y. Du, Effect of Cr content on microstructure characteristics and mechanical properties of ZrNbTaHf0. 2Crx refractory high entropy alloy, J. Alloy. Compd. 924 (2022) 166593, https://doi.org/10.1016/j.jallcom.2022.166593.
[21] L. Liu, J. Zhu, C. Zhang, J. Li, Q. Jiang, Microstructure and the properties of FeCoCuNiSnx high entropy alloys, Mater. Sci. Eng. A 548 (2012) 64–68, https://doi.org/10.1016/j.msea.2012.03.080.
[22] X. Wang, Y. Zhang, Y. Qiao, G. Chen, Novel microstructure and properties of multicomponent CoCrCuFeNiTix alloys, Intermetallics 15 (3) (2007) 357–362, https://doi.org/10.1016/j.intermet.2006.08.005.
[23] F.G. Coury, T. Butler, K. Chaput, A. Saville, J. Copley, J. Foltz, P. Mason, K. Clarke, M. Kaufman, A. Clarke, Phase equilibria, mechanical properties and design of quaternary refractory high entropy alloys, Mater. Des. 155 (2018) 244–256, https://doi.org/10.1016/j.matdes.2018.06.003.
[24] T. Ishimoto, N. Morita, R. Ozasa, A. Matsugaki, O. Gokcekaya, S. Higashino, M. Tane, T. Mayama, K. Cho, H.Y. Yasuda, M. Okugawa, Y. Koizumi, M. Yoshiya, D. Egusa, T. Sasaki, E. Abe, H. Kimizuka, N. Ikeo, T. Nakano, Superimpositional design of crystallographic textures and macroscopic shapes via metal additive manufacturing—Game-change in component design, Acta Mater. (2025) 120709, https://doi.org/10.1016/j.actamat.2025.120709.
[25] T. Mayama, T. Ishimoto, M. Tane, K. Cho, K. Manabe, D. Miyashita, S. Higashino, T. Kikukawa, H.Y. Yasuda, T. Nakano, Novel strengthening mechanism of laser powder bed fusion-manufactured Inconel 718: Effects of customized hierarchical interfaces, Addit. Manuf. 93 (2024) 104412, https://doi.org/10.1016/j.addma.2024.104412.
[26] K. Hagihara, T. Nakano, Control of anisotropic crystallographic texture in powder bed fusion additive manufacturing of metals and ceramics—a review, JOM 74 (4) (2022) 1760–1773, https://doi.org/10.1007/s11837-021-04966-7.
[27] Y.S. Kim, O. Gokcekaya, A. Matsugaki, R. Ozasa, T. Nakano, Laser energy-dependent processability of non-equiatomic TiNbMoTaW high-entropy alloy through in-situ alloying of elemental feedstock powders by laser powder bed fusion, Materialia 38 (2024) 102241, https://doi.org/10.1016/j.mtla.2024.102241.
[28] O. Gokcekaya, T. Ishimoto, Y. Nishikawa, Y.S. Kim, A. Matsugaki, R. Ozasa, M. Weinmann, C. Schnitter, M. Stenzel, H.S. Kim, Y. Miyabayashi, T. Nakano, Novel single crystalline-like non-equiatomic TiZrHfNbTaMo bio-high entropy alloy (BioHEA) developed by laser powder bed fusion, Mater. Res. Lett. 11 (4) (2023) 274–280, https://doi.org/10.1080/21663831.2022.2147406.
[29] T. Ishimoto, R. Ozasa, K. Nakano, M. Weinmann, C. Schnitter, M. Stenzel, A. Matsugaki, T. Nagase, T. Matsuzaka, M. Todai, Development of TiNbTaZrMo bio-high entropy alloy (BioHEA) super-solid solution by selective laser melting,

and its improved mechanical property and biocompatibility, Scr. Mater. 194 (2021) 113658, https://doi.org/10.1016/j.scriptamat.2020.113658.
[30] D. Lin, X. Xi, R. Ma, Z. Shi, H. Wei, X. Song, S. Hu, C. Tan, Fabrication of a strong and ductile FeCoCrNiMo0. 3 high-entropy alloy with a micro-nano precipitate framework via laser powder bed fusion, Composites Part B: Engineering 266 (2023) 111006, https://doi.org/10.1016/j.compositesb:2023.111006.
[31] J.-Y. Xu, C. Zhang, L.-X. Liu, R. Guo, M.-J. Sun, L. Liu, Achieving high strength in laser powder-bed fusion processed AlFeCuZr alloy via dual-nanoprecipitations and grain boundary segregation, J. Mater. Sci. Technol. 137 (2023) 56–66, https://doi.org/10.1016/j.jmst.2022.07.033.
[32] R. Acharya, J.A. Sharon, A. Staroselsky, Prediction of microstructure in laser powder bed fusion process, Acta Mater. 124 (2017) 360–371, https://doi.org/10.1016/j.actamat.2016.11.018.
[33] J. Xu, P. Kontis, R.L. Peng, J. Moverare, Modelling of additive manufacturability of nickel-based superalloys for laser powder bed fusion, Acta Mater. 240 (2022) 118307, https://doi.org/10.1016/j.actamat.2022.118307.
[34] P. Mohammadpour, H. Yuan, A. Phillion, Microstructure evolution of Inconel 625 alloy during single-track Laser Powder Bed Fusion, Addit. Manuf. 55 (2022) 102824, https://doi.org/10.1016/j.addma.2022.102824.
[35] W. Qi, W. Wang, X. Yang, G. Zhang, W. Ye, Y. Su, Y. Li, S. Chen, Effects of Al and Ti co-doping on the strength-ductility-corrosion resistance of CoCrFeNi-AlTi high-entropy alloys, J. Alloy. Compd. 925 (2022) 166751, https://doi.org/10.1016/j.jallcom.2022.166751.
[36] H. Cheng, H. Luo, X. Wang, X. Li, Microstructure and corrosion resistance properties of (FeCoNi) 86Al7Ti7 high-entropy alloy via different aging time, Corrosion Sci. (2023) 111670, https://doi.org/10.1016/j.corsci.2023.111670.
[37] H. Cheng, Z. Liu, H. Luo, Z. Pan, X. Wang, Q. Zhao, X. Qi, X. Li, Tuning the microstructure to improve corrosion resistance of additive manufacturing high-entropy alloy in proton exchange membrane fuel cells environment, Corrosion Sci. 213 (2023) 110969, https://doi.org/10.1016/j.corsci.2023.110969.
[38] V. Nguyen, M. Qian, Z. Shi, T. Song, L. Huang, J. Zou, Compositional design of strong and ductile (tensile) Ti-Zr-Nb-Ta medium entropy alloys (MEAs) using the atomic mismatch approach, Mater. Sci. Eng. A 742 (2019) 762–772, https://doi.org/10.1016/j.msea.2018.11.054.
[39] Y. Iijima, T. Nagase, A. Matsugaki, P. Wang, K. Ameyama, T. Nakano, Design and development of Ti–Zr–Hf–Nb–Ta–Mo high-entropy alloys for metallic biomaterials, Mater. Des. 202 (2021) 109548, https://doi.org/10.1016/j.matdes.2021.109548.
[40] D. Ma, M. Yao, K.G. Pradeep, C.C. Tasan, H. Springer, D. Raabe, Phase stability of non-equiatomic CoCrFeMnNi high entropy alloys, Acta Mater. 98 (2015) 288–296, https://doi.org/10.1016/j.actamat.2015.07.030.
[41] P. Wu, K. Gan, D. Yan, Z. Fu, Z. Li, A non-equiatomic FeNiCoCr high-entropy alloy with excellent anti-corrosion performance and strength-ductility synergy, Corrosion Sci. 183 (2021) 109341, https://doi.org/10.1016/j.corsci.2021.109341.
[42] Y.-J. Liang, L. Wang, Y. Wen, B. Cheng, Q. Wu, T. Cao, Q. Xiao, Y. Xue, G. Sha, Y. Wang, High-content ductile coherent nanoprecipitates achieve ultrastrong high-entropy alloys, Nat. Commun. 9 (1) (2018) 4063, https://doi.org/10.1038/s41467-018-06600-8.
[43] M. Cagirici, P. Wang, F.L. Ng, M.L.S. Nai, J. Ding, J. Wei, Additive manufacturing of high-entropy alloys by thermophysical calculations and in situ alloying, J. Mater. Sci. Technol. 94 (2021) 53–66, https://doi.org/10.1016/j.jmst.2021.03.038.
[44] P. Chen, S. Li, Y. Zhou, M. Yan, M.M. Attallah, Fabricating CoCrFeMnNi high entropy alloy via selective laser melting in-situ alloying, J. Mater. Sci. Technol. 43 (2020) 40–43, https://doi.org/10.1016/j.jmst.2020.01.002.
[45] P. Chen, C. Yang, S. Li, M.M. Attallah, M. Yan, In-situ alloyed, oxide-dispersion-strengthened CoCrFeMnNi high entropy alloy fabricated via laser powder bed fusion, Mater. Des. 194 (2020) 108966, https://doi.org/10.1016/j.matdes.2020.108966.
[46] E. Bassini, U. Galech, T. Soria, M. Aristizabal, I. Iturriza, S. Biamino, D. Ugues, Effect of the particle size distribution on physical properties, composition, and quality of gas atomized Astroloy powders for HIP application, J. Alloy. Compd. 890 (2022) 161631, https://doi.org/10.1016/j.jallcom.2021.161631.
[47] V. Golod, V.S. Sufiiarov, The evolution of structural and chemical heterogeneity during rapid solidification at gas atomization, IOP Conference Series: Materials Science and Engineering, IOP Publishing (2017) 012009, https://doi.org/10.1088/1757-899X/192/1/012009.
[48] H. Shi, Y. Zhao, H.-B. Gao, M.-S. Zhang, Y.-H. Jiang, F. Cao, J.-T. Zou, S.-H. Liang, In-situ spherical TiB2/Cu composite powder: A new method of liquid phase reaction coupled with gas atomization, Mater. Charact. 191 (2022) 112096, https://doi.org/10.1016/j.matchar.2022.112096.
[49] L. Farquhar, G. Maddison, L. Hardwick, F. Livera, I. Todd, R. Goodall, In-Situ Alloying of CoCrFeNiX High Entropy Alloys by Selective Laser Melting, Metals 12 (3) (2022) 456, https://doi.org/10.3390/met12030456.
[50] D. Lin, J. Hu, R. Wu, Y. Liu, X. Li, M.J. SaGong, C. Tan, X. Song, H.S. Kim, Multiscale plastic deformation in additively manufactured FeCoCrNiMox high-entropy alloys to achieve strength–ductility synergy at elevated temperatures, Int. J. Plast 183 (2024) 104142, https://doi.org/10.1016/j.ijplas.2024.104142.
[51] A. Grigoriev, I. Polozov, V. Sufiiarov, A. Popovich, In-situ synthesis of Ti2AlNb-based intermetallic alloy by selective laser melting, J. Alloy. Compd. 704 (2017) 434–442, https://doi.org/10.1016/j.jallcom.2017.02.086.
[52] W. Kong, S.C. Cox, Y. Lu, V. Villapun, X. Xiao, W. Ma, M. Liu, M.M. Attallah, The influence of zirconium content on the microstructure, mechanical properties, and biocompatibility of in-situ alloying Ti-Nb-Ta based β alloys processed by selective laser melting, Mater. Sci. Eng. C 131 (2021) 112486, https://doi.org/10.1016/j.msec.2021.112486.
[53] I. Polozov, A. Popovich, Microstructure and mechanical properties of niti-based eutectic shape memory alloy produced via selective laser melting in-situ alloying by nb, Materials 14 (10) (2021) 2696, https://doi.org/10.3390/ma14102696.
[54] X. Sun, M. Chen, T. Liu, K. Zhang, H. Wei, Z. Zhu, W. Liao, Characterization, preparation, and reuse of metallic powders for laser powder bed fusion: a review, Int. J. Extreme Manuf. (2023), https://doi.org/10.1088/2631-7990/acfbc3.
[55] J. Li, D. Ouyang, Q. Wang, Q. Teng, C. Cai, Q. Wei, Achieving superior tensile strength of CoCrFeNiTi0. 3 high-entropy alloy via in-situ laser powder bed fusion of CoCrFeNi and Ti, Mater. Sci. Eng. A 886 (2023) 145649, https://doi.org/10.1016/j.msea.2023.145649.
[56] C. Guo, S. Wei, Z. Wu, P. Wang, B. Zhang, U. Ramamurty, X. Qu, Effect of dual phase structure induced by chemical segregation on hot tearing reduction in additive manufacturing, Mater. Des. 228 (2023) 111847, https://doi.org/10.1016/j.matdes.2023.111847.
[57] M. Gäumann, C. Bezencon, P. Canalis, W. Kurz, Single-crystal laser deposition of superalloys: processing–microstructure maps, Acta Mater. 49 (6) (2001) 1051–1062, https://doi.org/10.1016/S1359-6454(00)00367-0.
[58] P. Kumar, O. Prakash, U. Ramamurty, Micro-and meso-structures and their influence on mechanical properties of selectively laser melted Ti-6Al-4V, Acta Mater. 154 (2018) 246–260, https://doi.org/10.1016/j.actamat.2018.05.044.
[59] O. Gokcekaya, T. Ishimoto, S. Hibino, J. Yasutomi, T. Narushima, T. Nakano, Unique crystallographic texture formation in Inconel 718 by laser powder bed fusion and its effect on mechanical anisotropy, Acta Mater. 212 (2021) 116876, https://doi.org/10.1016/j.actamat.2021.116876.
[60] M. Tane, K. Hagihara, M. Ueda, T. Nakano, Y. Okuda, Elastic-modulus enhancement during room-temperature aging and its suppression in metastable Ti–Nb-Based alloys with low body-centered cubic phase stability, Acta Mater. 102 (2016) 373–384, https://doi.org/10.1016/j.actamat.2015.09.030.
[61] M. Tane, S. Akita, T. Nakano, K. Hagihara, Y. Umakoshi, M. Niinomi, H. Nakajima, Peculiar elastic behavior of Ti–Nb–Ta–Zr single crystals, Acta Mater. 56 (12) (2008) 2856–2863, https://doi.org/10.1016/j.actamat.2008.02.017.
[62] K. Hagihara, M. Okubo, M. Yamasaki, T. Nakano, Crystal-orientation-dependent corrosion behaviour of single crystals of a pure Mg and Mg-Al and Mg-Cu solid solutions, Corrosion Sci. 109 (2016) 68–85, https://doi.org/10.1016/j.corsci.2016.03.019.
[63] T. Nagase, M. Todai, P. Wang, S.-H. Sun, T. Nakano, Design and development of (Ti, Zr, Hf)-Al based medium entropy alloys and high entropy alloys, Mater. Chem. Phys. 276 (2022) 125409, https://doi.org/10.1016/j.matchemphys.2021.125409.
[64] M.-H. Tsai, J.-H. Li, A.-C. Fan, P.-H. Tsai, Incorrect predictions of simple solid solution high entropy alloys: Cause and possible solution, Scr. Mater. 127 (2017) 6–9, https://doi.org/10.1016/j.scriptamat.2016.08.024.
[65] Y. Okazaki, S. Rao, Y. Ito, T. Tateishi, Corrosion resistance, mechanical properties, corrosion fatigue strength and cytocompatibility of new Ti alloys without Al and V, Biomaterials 19 (13) (1998) 1197–1215, https://doi.org/10.1016/S0142-9612(97)00235-4.
[66] F. Sun, J.-Y. Zhang, M. Marteleur, C. Brozek, E. Rauch, M. Veron, P. Vermaut, P. Jacques, F. Prima, A new titanium alloy with a combination of high strength, high strain hardening and improved ductility, Scr. Mater. 94 (2015) 17–20, https://doi.org/10.1016/j.scriptamat.2014.09.005.
[67] Y.-L. Zhou, M. Niinomi, Ti–25Ta alloy with the best mechanical compatibility in Ti–Ta alloys for biomedical applications, Mater. Sci. Eng. C 29 (3) (2009) 1061–1065, https://doi.org/10.1016/j.msec.2008.09.012.
[68] N. Li, X. Li, Z. Li, Q. Yu, Y. Zheng, Y. Hu, Q. Wang, C. Dong, Y. Jiang, X. Zhang, Differential effects of Zn and Co solutes on the properties of Cu–Ni–Sn alloys, Intermetallics 125 (2020) 106894, https://doi.org/10.1016/j.intermet.2020.106894.
[69] S.-H. Park, O. Gokcekaya, T. Nitomakida, T. Nakano, Effects of heat accumulation strategies on defects and microstructure of pure chromium fabricated by laser powder bed fusion: An experimental and numerical study, J. Mater. Res. Technol. 33 (2024) 7333–7344, https://doi.org/10.1016/j.jmrt.2024.11.049.
[70] Y. Hou, H. Su, H. Zhang, F. Li, X. Wang, Y. He, D. He, An integrated simulation model towards laser powder bed fusion in-situ alloying technology, Mater. Des. 228 (2023) 111795, https://doi.org/10.1016/j.matdes.2023.111795.
[71] K. Riener, N. Albrecht, S. Ziegelmeier, R. Ramakrishnan, L. Haferkamp, A. B. Spierings, G.J. Leichtfried, Influence of particle size distribution and morphology on the properties of the powder feedstock as well as of AlSi10Mg parts produced by laser powder bed fusion (LPBF), Addit. Manuf. 34 (2020) 101286, https://doi.org/10.1016/j.addma.2020.101286.
[72] A.B. Spierings, N. Herres, G. Levy, Influence of the particle size distribution on surface quality and mechanical properties in AM steel parts, Rapid Prototyping J. 17 (3) (2011) 195–202, https://doi.org/10.1108/13552541111124770.
[73] Y. Yang, D. Gu, D. Dai, C. Ma, Laser energy absorption behavior of powder particles using ray tracing method during selective laser melting additive manufacturing of aluminum alloy, Mater. Des. 143 (2018) 12–19, https://doi.org/10.1016/j.matdes.2018.01.043.
[74] M.A. Khimich, E.A. Ibragimov, V.V. Chebodaeva, K.A. Prosolov, A.I. Tolmachev, I.A. Glukhov, P.V. Uvarkin, N.A. Saprykina, A.A. Saprykin, Y.P. Sharkeev, From raw elements to 3D samples: An economical route for Co-Cr-Mo alloy fabrication, J. Alloy. Compd. 978 (2024) 173460, https://doi.org/10.1016/j.jallcom.2024.173460.

[75] J. Karimi, L. Kollo, R. Rahmani, P. Ma, Y. Jia, K. Prashanth, Selective laser melting of in-situ CoCrFeMnNi high entropy alloy: Effect of remelting, J. Manuf. Process. 84 (2022) 55–63, https://doi.org/10.1016/j.jmapro.2022.09.056.
[76] P. Pant, F. Salvemini, S. Proper, V. Luzin, K. Simonsson, S. Sjöström, S. Hosseini, R.L. Peng, J. Moverare, A study of the influence of novel scan strategies on residual stress and microstructure of L-shaped LPBF IN718 samples, Mater. Des. 214 (2022) 110386, https://doi.org/10.1016/j.matdes.2022.110386.
[77] F. Vecchiato, H. De Winton, P. Hooper, M. Wenman, Melt pool microstructure and morphology from single exposures in laser powder bed fusion of 316L stainless steel, Addit. Manuf. 36 (2020) 101401, https://doi.org/10.1016/j.addma.2020.101401.
[78] M.G. Norton, C. Suryanarayana, X-Ray diffraction: a practical approach, Springer, Boston (1998), https://doi.org/10.1007/978-1-4899-0148-4_1.
[79] Y. Waseda, E. Matsubara, K. Shinoda, X-ray diffraction crystallography: introduction, examples and solved problems, Springer Science & Business Media (2011), https://doi.org/10.1007/978-3-642-16635-8.
[80] T. Löffler, F. Waag, B. Gökce, A. Ludwig, S. Barcikowski, W. Schuhmann, Comparing the activity of complex solid solution electrocatalysts using inflection points of voltammetric activity curves as activity descriptors, ACS Catal. 11 (3) (2021) 1014–1023, https://doi.org/10.1021/acscatal.0c03313.
[81] A. Roy, P. Sreeramagiri, T. Babuska, B. Krick, P.K. Ray, G. Balasubramanian, Lattice distortion as an estimator of solid solution strengthening in high-entropy alloys, Mater. Charact. 172 (2021) 110877, https://doi.org/10.1016/j.matchar.2021.110877.
[82] U. Ulmer, K. Asano, A. Patyk, H. Enoki, Y. Nakamura, A. Pohl, R. Dittmeyer, M. Fichtner, Cost reduction possibilities of vanadium-based solid solutions–microstructural, thermodynamic, cyclic and environmental effects of ferrovanadium substitution, J. Alloy. Compd. 648 (2015) 1024–1030, https://doi.org/10.1016/j.jallcom.2015.07.110.
[83] D. Gu, C. Ma, M. Xia, D. Dai, Q. Shi, A multiscale understanding of the thermodynamic and kinetic mechanisms of laser additive manufacturing, Engineering 3 (5) (2017) 675–684, https://doi.org/10.1016/J.ENG.2017.05.011.
[84] N. Kang, W. Ma, L. Heraud, M. El Mansori, F. Li, M. Liu, H. Liao, Selective laser melting of tungsten carbide reinforced maraging steel composite, Addit. Manuf. 22 (2018) 104–110, https://doi.org/10.1016/j.addma.2018.04.031.
[85] J. Zhou, X. Han, H. Li, S. Liu, J. Yi, Investigation of layer-by-layer laser remelting to improve surface quality, microstructure, and mechanical properties of laser powder bed fused AlSi10Mg alloy, Mater. Des. 210 (2021) 110092, https://doi.org/10.1016/j.matdes.2021.110092.
[86] X. Liu, C. Zhao, X. Zhou, Z. Shen, W. Liu, Microstructure of selective laser melted AlSi10Mg alloy, Mater. Des. 168 (2019) 107677, https://doi.org/10.1016/j.matdes.2019.107677.
[87] W. Li, S. Li, J. Liu, A. Zhang, Y. Zhou, Q. Wei, C. Yan, Y. Shi, Effect of heat treatment on AlSi10Mg alloy fabricated by selective laser melting: Microstructure evolution, mechanical properties and fracture mechanism, Mater. Sci. Eng. A 663 (2016) 116–125, https://doi.org/10.1016/j.msea.2016.03.088.
[88] L. Thijs, K. Kempen, J.-P. Kruth, J. Van Humbeeck, Fine-structured aluminium products with controllable texture by selective laser melting of pre-alloyed AlSi10Mg powder, Acta Mater. 61 (5) (2013) 1809–1819, https://doi.org/10.1016/j.actamat.2012.11.052.
[89] C. Yan, L. Hao, A. Hussein, P. Young, J. Huang, W. Zhu, Microstructure and mechanical properties of aluminium alloy cellular lattice structures manufactured by direct metal laser sintering, Mater. Sci. Eng. A 628 (2015) 238–246, https://doi.org/10.1016/j.msea.2015.01.063.
[90] Z. Zarei, M. Zohrevand, A. Momeni, S. Sadeghpour, M. Somani, Effect of heat treatment regime on microstructure and phase evolution of AlMo0. 5NbTa0. 5TiZr refractory high entropy alloy, J. Alloy. Compd. 949 (2023) 169818, https://doi.org/10.1016/j.jallcom.2023.169818.
[91] G. Neumann, C. Tuijn, Self-diffusion and impurity diffusion in pure metals: handbook of experimental data, Elsevier, 2011.
[92] X. Min, S. Emura, X. Chen, X. Zhou, K. Tsuzaki, K. Tsuchiya, Deformation microstructural evolution and strain hardening of differently oriented grains in twinning-induced plasticity β titanium alloy, Mater. Sci. Eng. A 659 (2016) 1–11, https://doi.org/10.1016/j.msea.2016.01.105.
[93] X. Zhang, H. Andrä, S. Harjo, W. Gong, T. Kawasaki, A. Lutz, M. Lahres, Quantifying internal strains, stresses, and dislocation density in additively manufactured AlSi10Mg during loading-unloading-reloading deformation, Mater. Des. 198 (2021) 109339, https://doi.org/10.1016/j.matdes.2020.109339.
[94] C.N. Tomé, R.A. Lebensohn, Material Modeling With the Viscoplastic Self-Consistent (VPSC) Approach, Elsevier (2021), https://doi.org/10.1016/C2019-0-01217-4.
[95] D. Wang, Z. Wang, K. Li, J. Ma, W. Liu, Z. Shen, Cracking in laser additively manufactured W: Initiation mechanism and a suppression approach by alloying, Mater. Des. 162 (2019) 384–393, https://doi.org/10.1016/j.matdes.2018.12.010.
[96] O. Gokcekaya, T. Ishimoto, T. Todo, P. Wang, T. Nakano, Influence of powder characteristics on densification via crystallographic texture formation: Pure tungsten prepared by laser powder bed fusion, Addit. Manuf. Lett. 1 (2021) 100016, https://doi.org/10.1016/j.addlet.2021.100016.
[97] O. Gokcekaya, N. Hayashi, T. Ishimoto, K. Ueda, T. Narushima, T. Nakano, Crystallographic orientation control of pure chromium via laser powder bed fusion and improved high temperature oxidation resistance, Addit. Manuf. 36 (2020) 101624, https://doi.org/10.1016/j.addma.2020.101624.
[98] R.W. Messler Jr, Principles of welding: processes, physics, chemistry, and metallurgy, John Wiley & Sons, 2008.
[99] W. Shao, B. He, C. Qiu, Z. Li, Effect of hatch spacing and laser remelting on the formation of unique crystallographic texture of IN718 superalloy fabricated via laser powder bed fusion, Opt. Laser Technol. 156 (2022) 108609, https://doi.org/10.1016/j.optlastec.2022.108609.
[100] A. Chouhan, M. Hesselmann, A. Toenjes, L. Mädler, N. Ellendt, Numerical modelling of in-situ alloying of Al and Cu using the laser powder bed fusion process: A study on the effect of energy density and remelting on deposited track homogeneity, Addit. Manuf. 59 (2022) 103179, https://doi.org/10.1016/j.addma.2022.103179.
[101] J. Fu, H. Li, X. Song, M. Fu, Multi-scale defects in powder-based additively manufactured metals and alloys, J. Mater. Sci. Technol. 122 (2022) 165–199, https://doi.org/10.1016/j.jmst.2022.02.015.
[102] S. Kou, Solidification and liquation cracking issues in welding, JOM 55 (2003) 37–42, https://doi.org/10.1007/s11837-003-0137-4.
[103] Y. Wang, C. Yu, L. Xing, K. Li, J. Chen, W. Liu, J. Ma, Z. Shen, Grain structure and texture of the SLM single track, J. Mater. Process. Technol. 281 (2020) 116591, https://doi.org/10.1016/j.jmatprotec.2020.116591.
[104] M. Higashi, T. Ozaki, Selective laser melting of pure molybdenum: Evolution of defect and crystallographic texture with process parameters, Mater. Des. 191 (2020) 108588, https://doi.org/10.1016/j.matdes.2020.108588.
[105] M.C. Lam, S.C. Lim, H. Song, Y. Zhu, X. Wu, A. Huang, Scanning strategy induced cracking and anisotropic weakening in grain texture of additively manufactured superalloys, Addit. Manuf. 52 (2022) 102660, https://doi.org/10.1016/j.addma.2022.102660.
[106] B. Vrancken, R.K. Ganeriwala, A.A. Martin, M.J. Matthews, Microcrack mitigation during laser scanning of tungsten via preheating and alloying strategies, Addit. Manuf. 46 (2021) 102158, https://doi.org/10.1016/j.addma.2021.102158.
[107] I. Polozov, V. Sufiiarov, A. Kantyukov, N. Razumov, I. Goncharov, T. Makhmutov, A. Silin, A. Kim, K. Starikov, A. Shamshurin, Microstructure, densification, and mechanical properties of titanium intermetallic alloy manufactured by laser powder bed fusion additive manufacturing with high-temperature preheating using gas atomized and mechanically alloyed plasma spheroidized powders, Addit. Manuf. 34 (2020) 101374, https://doi.org/10.1016/j.addma.2020.101374.
[108] O. Gokcekaya, T. Ishimoto, T. Todo, R. Suganuma, R. Fukushima, T. Narushima, T. Nakano, Effect of scan length on densification and crystallographic texture formation of pure chromium fabricated by laser powder bed fusion, Crystals 11 (1) (2020) 9, https://doi.org/10.3390/cryst11010009.
[109] D. Wang, S. Wu, Y. Yang, W. Dou, S. Deng, Z. Wang, S. Li, The effect of a scanning strategy on the residual stress of 316L steel parts fabricated by selective laser melting (SLM), Materials 11 (10) (2018) 1821, https://doi.org/10.3390/ma11101821.
[110] X. Luo, T. Song, A. Gebert, K. Neufeld, I. Kaban, H. Ma, W. Cai, H. Lu, D. Li, N. Li, Programming crystallographic orientation in additive-manufactured beta-type titanium alloy, Adv. Sci. 10 (28) (2023) 2302884, https://doi.org/10.1002/advs.202302884.
[111] S.-H. Park, O. Gokcekaya, R. Ozasa, M.-H. Oh, Y.-W. Kim, H.S. Kim, T. Nakano, Microstructure and Crystallographic Texture Evolution of β-Solidifying γ-TiAl Alloy During Single-and Multi-track Exposure via Laser Powder Bed Fusion, Met. Mater. Int. (2023) 1–15, https://doi.org/10.1007/s12540-023-01579-4.
[112] M. Niinomi, T. Akahori, S. Katsura, K. Yamauchi, M. Ogawa, Mechanical characteristics and microstructure of drawn wire of Ti–29Nb–13Ta–4.6 Zr for biomedical applications, Mater. Sci. Eng. C 27(1) (2007) 154-161. https://doi.org/10.1016/j.msec.2006.04.008.
[113] P. Wang, Y. Feng, F. Liu, L. Wu, S. Guan, Microstructure and mechanical properties of Ti–Zr–Cr biomedical alloys, Mater. Sci. Eng. C 51 (2015) 148–152, https://doi.org/10.1016/j.msec.2015.02.028.
[114] E. Hall, The deformation and ageing of mild steel: III discussion of results, Proc. Phys. Soc. London, Sect. B 64 (9) (1951) 747, https://doi.org/10.1088/0370-1301/64/9/303.
[115] N.J. Petch, The cleavage strength of polycrystals, J. Iron Steel Inst. 174 (1953) 25–28.
[116] W.D. Bugbee, W.J. Culpepper, C.A. Engh, C.A. ENGH, Long-term clinical consequences of stress-shielding after total hip arthroplasty without cement, J. Bone Jt. Surg. 79(7) (1997) 1007-12.
[117] D. Sumner, Long-term implant fixation and stress-shielding in total hip replacement, J. Biomech. 48 (5) (2015) 797–800, https://doi.org/10.1016/j.jbiomech.2014.12.021.
[118] C.A. Engh, J.D. Bobyn, A.H. Glassman, Porous-coated hip replacement. The factors governing bone ingrowth, stress shielding, and clinical results, J. Bone Jt. Surg. 69(1) (1987) 45-55. https://doi.org/10.1302/0301-620X.69B1.3818732.
[119] M. Kaur, K. Singh, Review on titanium and titanium based alloys as biomaterials for orthopaedic applications, Mater. Sci. Eng. C 102 (2019) 844–862, https://doi.org/10.1016/j.msec.2019.04.064.
[120] M. Balazic, J. Kopac, M.J. Jackson, W. Ahmed, Titanium and titanium alloy applications in medicine, Int. J. Nano Biomater. 1 (1) (2007) 3–34, https://doi.org/10.1504/IJNBM.2007.016517.
[121] C. Aguilar, C. Salvo, J. Henriquez, D. Vega, I. Alonso, L. Muñoz, Computational analysis of the graded porosity distribution on the elastic modulus of Ti foams, Mater. Today Commun. (2023) 106391, https://doi.org/10.1016/j.mtcomm.2023.106391.
[122] J. Feng, D. Wei, P. Zhang, Z. Yu, C. Liu, W. Lu, K. Wang, H. Yan, L. Zhang, L. Wang, Preparation of TiNbTaZrMo high-entropy alloy with tunable Young's modulus by selective laser melting, J. Manuf. Process. 85 (2023) 160–165, https://doi.org/10.1016/j.jmapro.2022.11.046.

[123] P. Wang, M. Todai, T. Nakano, Beta titanium single crystal with bone-like elastic modulus and large crystallographic elastic anisotropy, J. Alloy. Compd. 782 (2019) 667–671, https://doi.org/10.1016/j.jallcom.2018.12.236.
[124] M. Tane, S. Akita, T. Nakano, K. Hagihara, Y. Umakoshi, M. Niinomi, H. Mori, H. Nakajima, Low Young's modulus of Ti–Nb–Ta–Zr alloys caused by softening in shear moduli c′ and c44 near lower limit of body-centered cubic phase stability, Acta Mater. 58 (20) (2010) 6790–6798, https://doi.org/10.1016/j.actamat.2010.09.007.
[125] E.P. George, D. Raabe, R.O. Ritchie, High-entropy alloys, Nat. Rev. Mater. 4 (8) (2019) 515–534, https://doi.org/10.1038/s41578-019-0121-4.
[126] J. Feng, Y. Tang, J. Liu, P. Zhang, C. Liu, L. Wang, Bio-high entropy alloys: Progress, challenges, and opportunities, Front. Bioeng. Biotechnol. 10 (2022) 977282, https://doi.org/10.3389/fbioe.2022.977282.
[127] L. Chang, H. Jing, C. Liu, C. Qiu, X. Ling, High-Entropy Materials for Prospective Biomedical Applications: Challenges and Opportunities, Adv. Sci. 11 (42) (2024) 2406521, https://doi.org/10.1002/advs.202406521.
[128] E. Eisenbarth, D. Velten, K. Schenk-Meuser, P. Linez, V. Biehl, H. Duschner, J. Breme, H. Hildebrand, Interactions between cells and titanium surfaces, Biomol. Eng. 19 (2–6) (2002) 243–249, https://doi.org/10.1016/S1389-0344(02)00032-1.
[129] C.S. Chen, M. Mrksich, S. Huang, G.M. Whitesides, D.E. Ingber, Geometric control of cell life and death, Science 276 (5317) (1997) 1425–1428, https://doi.org/10.1126/science:276.5317.1425.
[130] A. Mahapatro, Bio-functional nano-coatings on metallic biomaterials, Mater. Sci. Eng. C 55 (2015) 227–251, https://doi.org/10.1016/j.msec.2015.05.018.